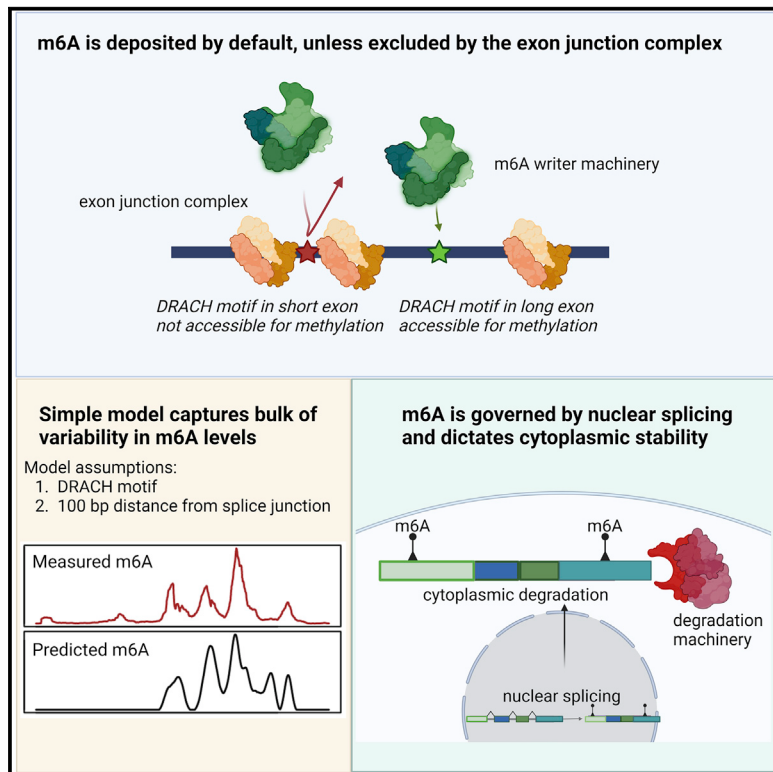


Exclusion of m6A from splice-site proximal regions by the exon junction complex dictates m6A topologies and mRNA stability

Graphical abstract



Authors

Anna Uzonyi, David Dierks,
Ronit Nir, ..., Hervé Le Hir,
Boris Slobodin, Schraga Schwartz

Correspondence

boris.sl@technion.ac.il (B.S.),
schwartz@weizmann.ac.il (S.S.)

In brief

Uzonyi et al. find that m6A is introduced by default at all eligible consensus motifs, except near splice sites, where it is occluded via the exon junction complex. A simple model, relying on motif availability and splice-site distance *in silico* reconstructs m6A topologies. m6A links exon-intron architecture with cytoplasmic fate.

Highlights

- m6A is deposited by default at DRACH motifs but excluded from splice-site proximity
- Simple model based on above principles *in silico* reconstructs m6A landscapes
- Exclusion from splice-junction proximity is mediated via exon junction complex
- m6A is memory of nuclear splicing dictating cytoplasmic stability



Article

Exclusion of m6A from splice-site proximal regions by the exon junction complex dictates m6A topologies and mRNA stability

Anna Uzonyi,¹ David Dierks,¹ Ronit Nir,¹ Oh Sung Kwon,^{2,6} Ursula Toth,³ Isabelle Barbosa,² Cindy Burel,² Alexander Brandis,⁴ Walter Rossmanith,³ Hervé Le Hir,² Boris Slobodin,^{1,5,*} and Schraga Schwartz^{1,7,*}

¹Department of Molecular Genetics, Weizmann Institute of Science, Rehovot 7630031, Israel

²Institut de Biologie de l'Ecole Normale Supérieure (IBENS), Ecole Normale Supérieure, CNRS, INSERM, Université PSL, 75005 Paris, France

³Center for Anatomy & Cell Biology, Medical University of Vienna, 1090 Vienna, Austria

⁴Life Sciences Core Facilities, Weizmann Institute of Science, Rehovot 7630031, Israel

⁵Department of Biochemistry, Rappaport Faculty of Medicine, Technion - Israel Institute of Technology, Haifa 31096, Israel

⁶Present address: BioResearch center, Samsung biologics, 300, Songdo bio-daero, Yeonsu-gu, Incheon 21987, South Korea

⁷Lead contact

*Correspondence: boris.sl@technion.ac.il (B.S.), schwartz@weizmann.ac.il (S.S.)

<https://doi.org/10.1016/j.molcel.2022.12.026>

SUMMARY

N6-methyladenosine (m6A), a widespread destabilizing mark on mRNA, is non-uniformly distributed across the transcriptome, yet the basis for its selective deposition is unknown. Here, we propose that m6A deposition is not selective. Instead, it is exclusion based: m6A consensus motifs are methylated by default, unless they are within a window of ~100 nt from a splice junction. A simple model which we extensively validate, relying exclusively on presence of m6A motifs and exon-intron architecture, allows *in silico* recapitulation of experimentally measured m6A profiles. We provide evidence that exclusion from splice junctions is mediated by the exon junction complex (EJC), potentially via physical occlusion, and that previously observed associations between exon-intron architecture and mRNA decay are mechanistically mediated via m6A. Our findings establish a mechanism coupling nuclear mRNA splicing and packaging with the covalent installation of m6A, in turn controlling cytoplasmic decay.

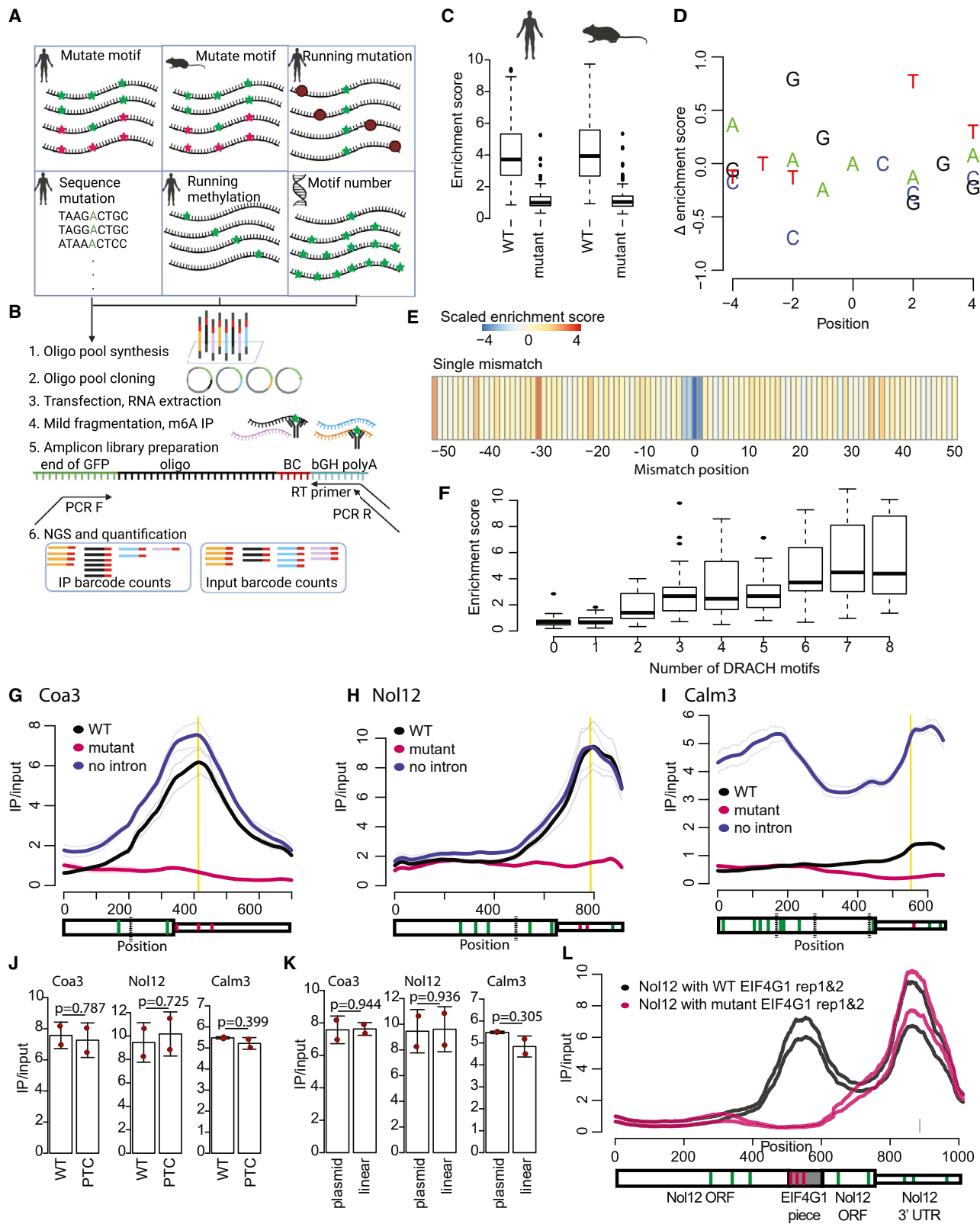
INTRODUCTION

N6-methyladenosine (m6A) is the most widespread modification on mRNA, present at roughly 0.2–0.4% of all adenosines.¹ m6A is installed at a consensus motif, whose core is typically represented as a DRACH motif (D = A/G/T, R = A/G, H = A/C/T), which also extends into adjacent nucleotides.^{2,3} Yet, a major feature of m6A distribution not accounted for by sequence is the strong positional enrichment of m6A within genes. m6A was originally described as being enriched within atypically long internal exons and near stop codons.^{4,5} A subsequent study suggested that rather than being associated with the stop codon, m6A was associated with the last intron-exon junction within a gene.⁶ This prompted multiple studies to explore a potential impact of methylation on splicing, whereby only weak effects were typically observed.^{7–9} In parallel, alternative potential mechanisms underlying the biased distribution of m6A have been proposed, invoking chromatin marks biased toward the ends of genes and potential involvement of the transcription termination machinery.^{6,10,11} However, none of the proposed mechanisms accounts for the enrichment of m6A near stop codons, nor near

last exons nor within long internal exons. The highly biased distribution of m6A has thus remained enigmatic, and the mechanism underlying it largely unknown. Given that m6A plays a well-established role in directing cytoplasmic degradation of mRNA,^{12–15} elucidating the forces shaping m6A is pivotal for obtaining a complete understanding of the rules governing mRNA stability.

mRNA levels are shaped by production and degradation. Intriguingly, diverse studies have consistently found that mRNA degradation rates correlate most strongly with “exon density,” a ratio between the number of exons within the coding region and the coding region length,^{16–20} explaining nearly 30% of the variability in degradation rates between different genes.¹⁶ While this observation suggests a strong connection between exon-intron architecture and RNA stability, its mechanistic basis is unknown. Exon-intron architecture of genes has also been associated with additional features of genes including RNA processing, export, and translation.^{21–26} The underlying mechanisms are poorly understood, whereby a key gap in our understanding is how the history of splicing in the nucleus is encoded to subsequently drive cytoplasmic fate.





(legend on next page)

In addition to intron excision, splicing also has a considerable impact on messenger ribonucleoprotein (mRNP) particle structure. Assembled during splicing and deposited upstream of exon-exon junctions, the exon junction complex (EJC) is a stable molecular mark of splicing.^{27,28} The core of this multimeric complex comprises the RNA helicase eIF4A3, the hetero-dimer MAGOH-Y14, and MLN51. The EJC core accompanies mRNAs to the cytoplasm and serves as a binding platform for a dozen of more peripheral factors. Recent structural and biochemical studies revealed that pre-translational mRNPs adopt a compact and elongated rod-like structure^{29–31} suggesting that RNA-binding proteins (RBPs) including EJCs contribute to mRNA packaging. Functionally, the EJC has been found to link pre-mRNA splicing to downstream events including mRNA transport, localization, translation, and surveillance,^{28,32} yet the underlying mechanisms remain incompletely understood, in particular given that the EJCs are disassembled during mRNA translation.³³

Here, we explore the basis for the region-specific distribution of m6A. We reveal that the transcriptome-wide selectivity in m6A deposition is not inclusion-based, but rather exclusion based. We suggest that sites harboring an m6A consensus sequence are methylated by default, unless they are within a window of up to ~100 nucleotides (nt) from a splice junction, in which case their formation is inhibited by the EJC. We further provide evidence that m6A—installed in a splice-junction-sensitive manner—serves as the mechanism connecting exon-intron architecture with cytoplasmic decay. Our findings thus causally link mRNA splicing and EJC deposition with the covalent installation of m6A in the nucleus, which—in turn—subsequently controls the mRNA cytoplasmic stability.

RESULTS

Dissection of sequence determinants of m6A deposition

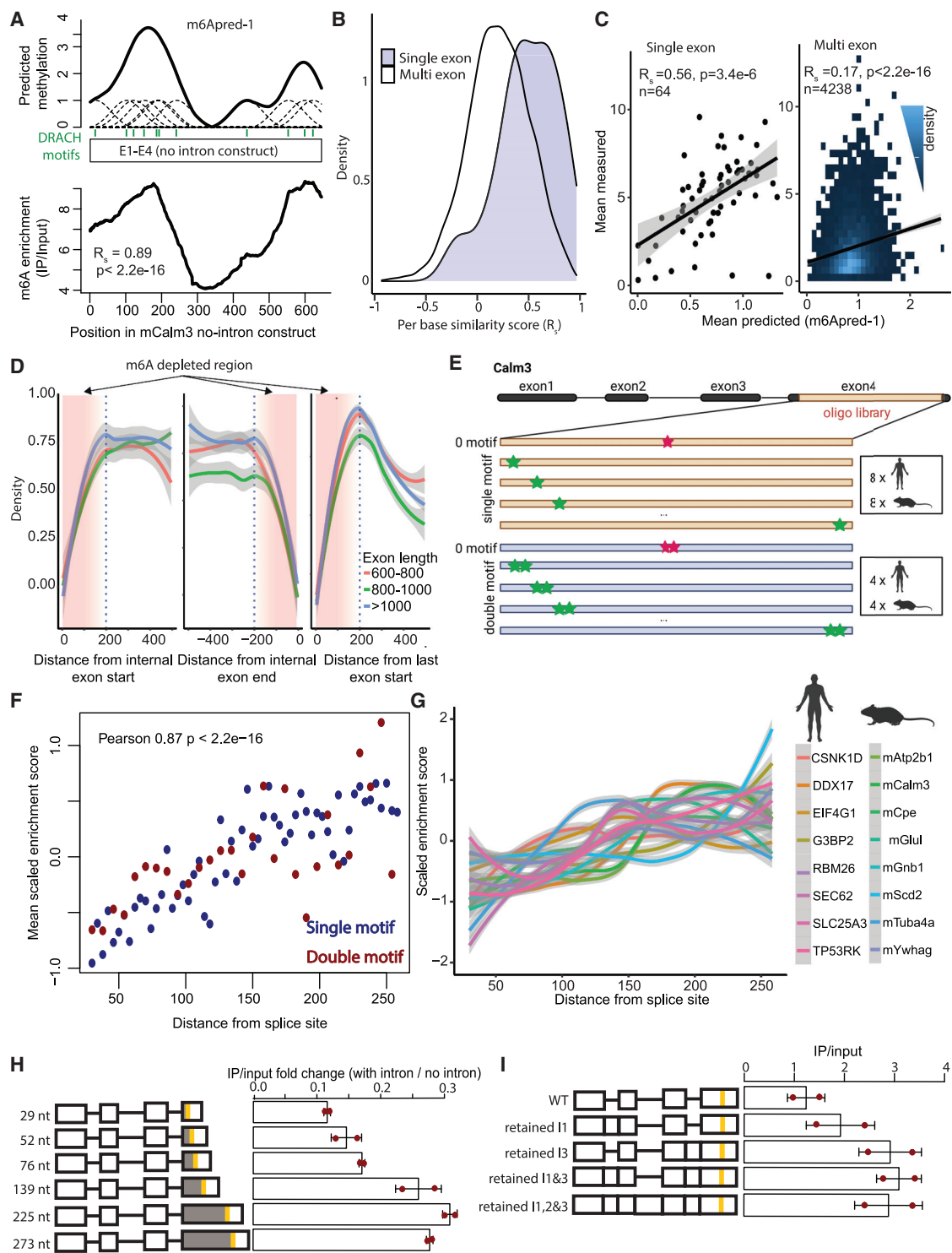
M6A is strongly enriched at long internal exons and last exons, near stop codons, yet the m6A consensus (“DRACH”) motif is not enriched in these regions (Figure S1A), suggesting additional sources of specificity. To systematically assay the determinants

governing m6A specificity, we established a massively parallel reporter assay, allowing us to interrogate the methylation status of 7,584 different sequences, each 101 base pairs (bp) in length. These sequences were designed to include (1) wild-type (WT) and point-mutated DRACH motifs embedded within high-confidence m6A sites residing within human or mouse genes, (2) systematic mutations of each of the positions along a methylated sequence, (3) systematic shifting of the relative position of DRACH motifs along sequences, and (4) synthetic sequences comprising varying number of DRACH motifs (Figure 1A). All sequences were cloned as a pool downstream of green fluorescent protein (GFP) and the resulting plasmids were transfected into HEK293T cells, following which m6A was monitored via m6A immunoprecipitation (IP) and targeted amplification (Figure 1B). Each sequence was assigned an enrichment score, capturing the fold-change in read-count in m6A-IP samples in comparison to an “input” control. Enrichment scores were highly reproducible internally (Pearson R [R_p] = 0.95) (Figure S1B), as evaluated on the basis of 150 sequences that had been integrated twice into the pool with different barcodes, and were also reproducible between biological replicates (R_p = 0.82) (Figure S1C).

Reassuringly, enrichment scores were considerably higher in WT sequences than in mutated counterparts (Figure 1C). In addition, an analysis of the systematically mutated series allowed us to *de novo functionally* reconstruct the requirement for a DRACH motif, which has previously been characterized primarily based on associative analysis (Figure 1D). However, these analyses failed to uncover any new requirement for methylation: sequences were methylated at roughly uniform levels regardless of their relative location within a sequence (Figure S1D), and no sequences appeared to be required beyond the positions harboring the m6A consensus motif (Figures 1E and S1E). Perhaps most surprisingly, we found that even the completely synthetic sequences were enriched in a manner correlating with the number of synthetic DRACH motifs installed in them (Figure 1F). These experiments thus suggested that under the surveyed contexts, a DRACH motif is not only required for methylation but may potentially also be sufficient.

Figure 1. Interrogation of factors controlling m6A specificity

- (A) Depiction of the library subsets analyzed in Figures 1 and S1.
- (B) Experimental pipeline of the m6A measurement of the oligo library pool (see STAR Methods).
- (C) Enrichment score of WT and mutant sequences on the basis of 200 human and 200 mouse sequences. Outliers with an enrichment score over 10 are not shown. Boxplots correspond to the median, Q1 and Q3, whiskers mark Q1 – 1.5 IQR and Q3 + 1.5 IQR.
- (D) Delta (Δ) enrichment scores of the motif sequence set on the basis of permutation of the extended 9-mer consensus motif in four human mut-secondary sequences. The methylated A corresponds to position 0. Each value is a mean of all sequences with a certain base at a given position.
- (E) Heatmap of enrichment Z-scores in the running single-nucleotide point-mutation series.
- (F) m6A Enrichment (y axis) as a function of the number of synthetic DRACH motifs, ranging from 0 to 8. Each box is based on 18 synthetic sequences with different extended 9-mer consensus motifs. Boxplots correspond to the median, Q1 and Q3, whiskers mark Q1 – 1.5 IQR and Q3 + 1.5 IQR.
- (G) Top: IP/input ratio over the Coa3 coding region and 3' UTR. Thin lines: measurements (two replicates). Thick lines—average with a 10% Loess fitting. Bottom: thick box—CDS, thin box—3' UTR. Black dotted lines—exon-intron junctions. Green and red stripes—eligible DRACH motifs, where the red ones were mutated in the mutant constructs and the green ones were left unchanged. Vertical yellow stripe—main DRACH motif.
- (H and I) Measurements for Nol12 (H) and Calm3 (I), as in (G).
- (J) IP/input ratios at the methylated site across each of the three constructs in the WT sequences (lacking an intron) in comparison to counterparts into which a premature termination codon (PTC) was introduced. All constructs lack introns. Red dots mark individual measurements; the height of the bars mark the average and the whiskers represent the SD of the mean. P-values for two-tailed Student's *t* test are shown.
- (K) IP/input ratios at the methylated site across each of the three constructs in the WT constructs (lacking an intron) which were transfected as plasmids vs. linear DNA into cells, represented as in (J).
- (L) IP/input coverage of constructs with a 101-nt-long *Eif4G1*-derived piece (WT or DRACH-depleted mutant) cloned within the open reading frame (ORF) of the intron-less *Nol12* gene. Based on two biological replicates. The gene model (bottom) is depicted as in (G).

**Figure 2. Proximity to intron-exon junctions inhibits m6A formation**

(A) (Top) depiction of m6Apred-1 predictions on the basis of the *Calm3* gene. Every eligible DRACH motif (depicted as green bars) is modeled as a Gaussian, whereby the sum of all Gaussians overlapping a position defines its predicted methylation level. (Bottom) measured IP/input values along the *Calm3* gene are shown. The indicated correlation reflects the per-base correlation between the predicted (top) and measured (bottom) levels of methylation along the *Calm3* gene.

(B) Distribution of PBSSs within single-exon and multi-exon genes.

(C) Correlation between the mean predicted levels of methylation (mean m6Apred-1 values along gene bodies) and corresponding measurements (IP/input in A549 cells), shown for both single-exon and multi-exon genes. Spearman correlation coefficient and p-value are marked on the figure.

(legend continued on next page)

We next speculated that the basis for m6A selectivity might reside within more distal elements, such as the reading frame or intron-exon architecture. Motivated by the enrichment of m6A in internal and last exons, we sought to assess whether RNA splicing is required for methylation. We selected three mouse genes with well-supported m6A sites in the stop codon vicinity and with a relatively short last intron: *Coa3*, *No12*, and *Calm3*. The exons encoding each of the genes, in addition to the last intron (preceding the methylation site) were cloned into plasmids either in their WT form or with point mutation of the suspected methylation motifs (“point-mut”). In addition, the same sequences were cloned without introns (“no-intron”). In one of the 3 cases (“*Calm3*”) the introns were sufficiently short to enable us to include three introns. Application of m6A-seq²¹ to all 9 constructs, following their transfection into human MCF7 cells, revealed that the WT constructs recapitulated the “stop-codon” proximal enrichment of the endogenous constructs (Figures 1G–I and S1F), which was dramatically reduced in the point-mutated counterparts (Figures 1G–I and S1G). Similar profiles were observed for transiently expressed constructs and stably integrated counterparts (Figure S1H). However, no reduction was observed in the intron-less constructs; indeed, increased methylation levels were observed in two out of the three cases (Figures 1G–I and S1G). These results thus indicate that splicing is not a prerequisite for methylation. Given the association of m6A peaks with stop codons, we next assessed whether an intact reading frame was required for methylation. Introduction of a premature stop-codon into all three no-intron constructs gave rise to nearly identical methylation levels as their WT counterparts (Figure 1J), ruling out a requirement for a reading frame. We further found that methylation profiles were similar when DNA was transfected as a (circular) plasmid, or in a linear form, following PCR amplification from the plasmid (Figures 1K and S1I), suggestive of a relative indifference to chromatin properties. Finally, we found that introduction of a 101-bp methylated region from the 3' UTR of *EIF4G1* into the gene body of the *No12* no-intron construct led to strong methylation of the *EIF4G1* site (Figure 1L). This result demonstrates that presence within a 3' gene region is not a requirement for methylation and—once again—pointed at DRACH motifs potentially

being sufficient for inducing methylation, rendering the question of the determinants giving rise to the region-specific deposition of m6A all the more enigmatic.

An m6A exclusion zone in the proximity of splice junctions

In the above experiment we noted that removal of introns led to increased m6A signal (Figures 1G–I and S1G). This was particularly pronounced in the case of the *Calm3* construct. Whereas enrichment was apparent only in the 3' UTR in the intron-harboring construct, in the intron-lacking counterpart, substantial enrichment was apparent over the beginning of the CDS in a region harboring a high density of DRACH sites (Figure 1I). The enrichment pattern within the intron-less construct which appeared to mirror DRACH density led us to wonder whether it could be predicted *in silico* simply on the basis of DRACH sites along it. To explore this, we established a simple model of m6A formation (“m6Apred-1”) according to which every “eligible” m6A site is methylated at a fixed level. Eligible m6A sites were defined as ones harboring any of the seven most prevalent consensus sequences (GGACC, AGACA, TGACT, AGACT, GAACT, GGACA, and GGACT).³⁴ To allow for a direct comparison between our model and m6A-seq, in which the signal of an m6A site is spread as a “peak” over a window surrounding the methylated site, we modeled each predicted m6A site as a Gaussian distribution centered over a 200-bp window surrounding the methylation site. The predicted methylation level of each position was defined as the sum of predicted signal overlapping that position (Figure 2A, top). Remarkably, the m6Apred-1 predicted methylation profile for *Calm3* displayed an excellent correlation with measurements in the intron-less context (Spearman $R_s = 0.89$, $p < 2.2e-16$) (Figure 2A, bottom) but no correlation with the corresponding measurements in the intron-harboring context ($R_s = -0.06$, $p = 0.1$). Of note, the *in silico* reconstituted methylation profile in *Calm3* is based on 11 different eligible DRACH motifs distributed along the length of this gene, all of which are predicted to undergo methylation by this model.

To explore whether DRACH-motif distribution along genes was sufficient for predicting methylation patterns in intron-less

(D) Frequency of detected m6A sites as a function of distance from the start (left) or end (middle) of internal exons, or from the start of the last exon (right). Blue dashed line marks 200-bp distance from the nearest exon-intron junction.

(E) Schematic of the long oligo pool planning. Oligo pool containing a single motif and a double-motif set, with DRACH motifs moved from the beginning to the end of the sequence was cloned to the last exon of *Calm3*. The sequences are based on human and mouse sequences of the indicated numbers (right boxes). Green stars mark DRACH motifs, red stars mark mutated DRTCH motifs.

(F) Correlation of the mean enrichment score of different sequences with the relative position compared to the exon-intron junction. Enrichment scores were scaled within the sequences. Pearson correlation coefficient and p value are indicated.

(G) Plot showing the scaled enrichment score for each of the natural (human and mouse) single-motif constructs.

(H) Left: schematic of constructs with different distances between the last splice junction and the strong 3' m6A motif, on the basis of the *Calm3* gene. Vertical yellow lines mark the position of the quantified DRACH motif. The distance between the quantified 3' UTR DRACH motif and the last splice junction is marked in gray. Right: bar plot comparing the methylation levels of the 3' UTR DRACH site of the WT *Calm3* construct, and corresponding constructs with reduced or increased distance between the last splice junction and the quantified site. For the quantification of input and IP signal, only reads beginning at most 10 bp upstream of the modification site were used to avoid contribution of a signal from a more upstream consensus motif (see STAR Methods). Quantification shows the ratio of enrichment between the intron harboring and intron-less constructs. Red dots mark individual measurements, the heights of the bars mark the average, and the whiskers represent the SD of the mean.

(I) Left: schematic of constructs retaining introns 1, 3, 1 and 3, or all on the basis of the *Calm3* gene. All graphical parameters are according to (E). Right: bar plots comparing the methylation levels of the 3' UTR DRACH site of the WT *Calm3* construct, as well as corresponding constructs with retention of intron 1; 3; 1 and 3; or 1, 2, and 3. Red dots mark individual measurements, the height of the bars mark the average, and the whiskers represent the SD of the mean. For the quantification, 5' read starts up to 40 nt upstream were summed.

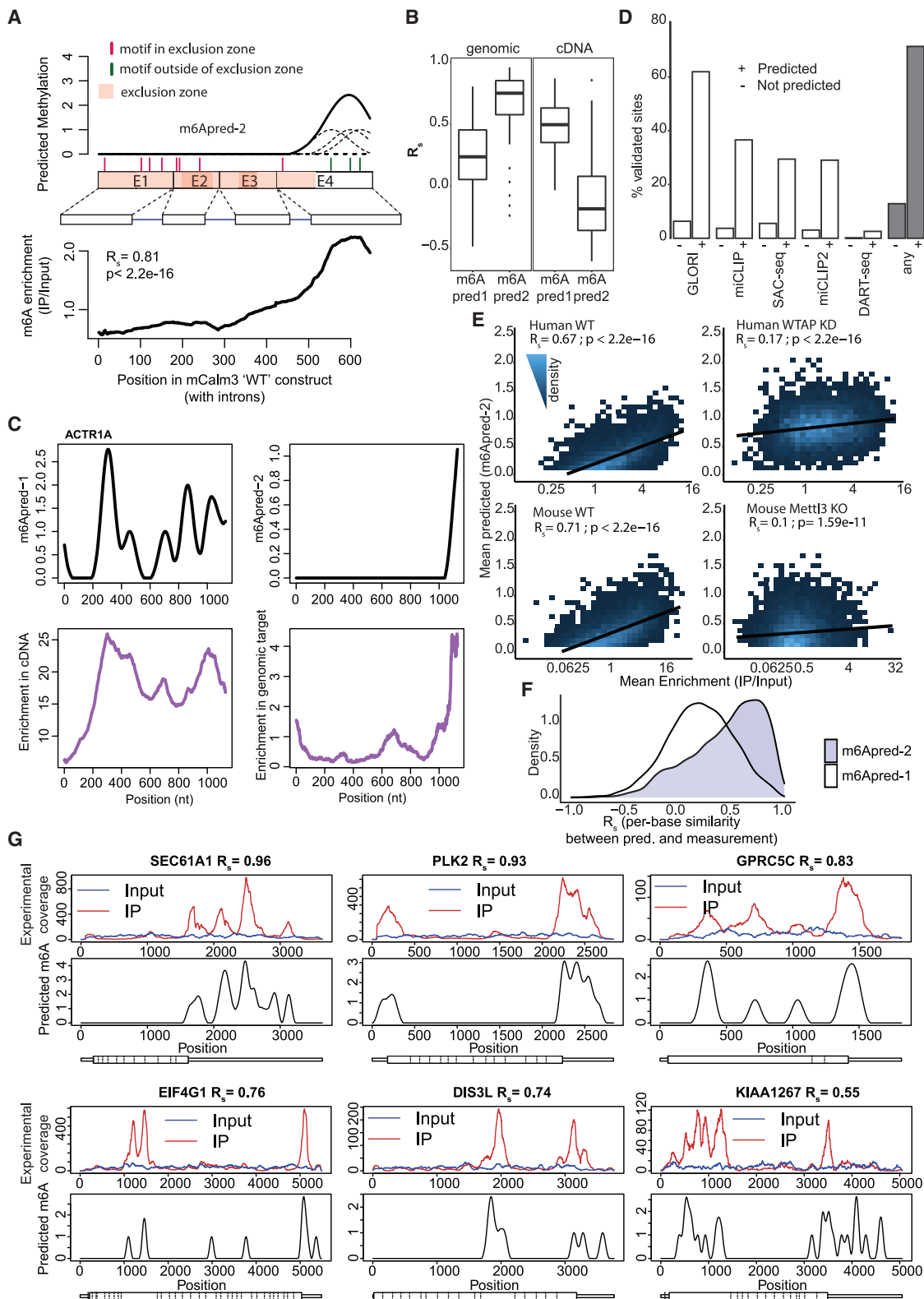


Figure 3. M6A topologies can be predicted de novo based on motif and exon-intron architecture

(A) (Top) development of m6Apred-2, relying on eligible DRACH motifs and exon-intron architecture, illustrated on the basis of the *Calm3* gene. Eligible m6A sites are depicted as lines, drawn in red if they are within an m6A exclusion zone (within 100 bp of an exon-intron junction, depicted as a transparent box in peach) or

(legend continued on next page)

genes transcriptome-wide, we applied m6Apred-1 to ~20,000 human gene models and compared its predictions against m6A signal from human A549 cells.³⁴ To explore agreement between predicted and measured methylation levels *within* genes, we established a “per-base similarity score” (PBSS), capturing the per-base Spearman correlation between predicted and measured (IP, input) profiles. Consistently with our above results, we found that variability *within* genes was well captured by m6Apred-1 in intron-lacking genes (median PBSS = 0.5, n = 64) but not in intron-harboring ones (median PBSS = 0.21, n = 4,238) (Figure 2B). Also, variability *between* genes, assessed by correlating the mean predicted vs. measured m6A level per genes, were well captured in intron-lacking genes ($R_s = 0.56$) but poorly in intron-harboring counterparts ($R_s = 0.17$) (Figure 2C). These results thus suggest that in the absence of introns, m6A accumulation to a large extent mirrors the distribution of methylation consensus sequences and that introns have an inhibitive impact on m6A formation.

To explore the possibility of an inhibitive effect of introns on methylation, we examined the distribution of 81,518 methylation sites, identified in human cells at single-nucleotide resolution by six m6A-miCLIP experiments,³⁵ with respect to the intron-exon junction. Remarkably, we found that m6A depleted from both the 5' AND 3' ends of long internal exons, as well as from the 5' of last exons, plateauing at a distance of ~200 nt from splice junctions (Figures 2D and S2A–S2D). The size of this “m6A exclusion zone” was fixed and did not depend on the length of the internal exon (Figures 2D and S2B). Similar results were obtained on the basis of 25,879 m6A sites identified via miCLIP in mice³⁶ (Figure S2C) as well as upon analysis of DART-seq data³⁷ (Figure S2D). These results thus suggest the relative depletion of methylation sites from splice junctions, extending previous findings.¹⁴

To establish that distance from the junction causally impacts m6A formation, we selected sixteen 239-bp regions harboring a prominent methylation site originating from different human and mouse genes (Figure 2E). For each of these methylation sites, we designed a series of 58 variants in which we systematically shifted the position of either a single or two consecutive methylation consensus motifs in 4-nt increments. These oligos were synthesized as a pool and cloned into the last exon of the Calm3 construct, such that the relative distance of the methylation consensus motif from the last exon/intron junction spanned

the range from 30 to 258 bp (Figure S2E–S2G). Remarkably, a continuous and pronounced increase in methylation was observed with increased distance from the splice junction across nearly every target (Figures 2F, 2G, and S2H), confirming the causal role of distance from splice site in controlling methylation levels. Further support was obtained on the basis of a series of perturbations conducted on the Calm3 gene, involving modulation of the distance between the *Calm3* methylation site and the last intron-exon junction. We found that increasing the distance between the methylation site and the splice junction gave rise to increased relative levels, up to a distance of 225 bp as measured both by m6A-seq (Figure 2H) and by SCARLET³⁸ (Figure S2I). We further confirmed that introduction of a 5-bp deletion at the donor site of intron 3, which led to intron 3 retention (Figures 2I and S2J), thereby increasing the distance of the methylated DRACH motif from a splice junction, which gave rise to increased m6A levels, whereas retention of intron 1 led to a much more reduced effect (Figure 2I).

Transcriptome-wide m6A topologies are predictably driven via exclusion from splice junctions

The above results prompted us to explore the following model: rather than assuming that methylation is *off* by default and seeking elements driving its specificity, we considered an opposite model in which methylation is *on* by default on all DRACH motifs *unless* it is in proximity to a splice junction. To assess whether a consensus sequence and a minimal distance from a splice junction are sufficient for *in silico* reconstitution of m6A landscapes, we developed “m6Apred-2,” incorporating two considerations: (1) Every “eligible” m6A site is methylated (as in m6Apred-1), (2) unless it is within an “m6A exclusion zone,” a region spanning a fixed size (“ExclusionZoneSize”) from the exon/intron junction (Figures 3A [top] and S3A–S3C). While the region depleted of m6A was roughly 200 nt long, the extent of depletion dropped continuously with distance from the junction (Figure 2D); hence, the ExclusionZoneSize was set at 100 nt, roughly midway within the depleted region (Figure 2D). Of note, for intron-less genes, m6Apred-1 and m6Apred-2 predictions are identical. Encouragingly, when we applied m6Apred-2 to the intron-harboring version of *Calm3*, the constraint on distance from a junction only allowed 3 (of the 11) DRACH motifs to undergo methylation, all of which were in the last (long) exon. This resulted in a high agreement with experimental

green otherwise. Each site is modeled as a Gaussian model, and the sum of the Gaussians at each position define its predicted levels of methylation. (Bottom) measurements of m6A (IP/input) for the WT *Calm3* construct (harboring agreement). The depicted correlation is the per-base correlation between the measured levels and the predicted ones (top).

(B) Boxplot of m6Apred-1 and m6Apred-2 correlation with measured m6A for 33 expressed cDNA constructs and their endogenous counterparts. For cDNA-based predictions the correlations are performed across the ORF; for genomic counterparts the correlations are across the gene bodies. Boxplots correspond to the median, Q1, and Q3; whiskers mark Q1 – 1.5 IQR and Q3 + 1.5 IQR.

(C) An example of observed and predicted methylation in cDNA constructs and endogenous counterparts.

(D) Predicted methylation levels are confirmed by experimental approaches. For each of ~120,000 sites across ~7,000 genes, the fraction of sites within gene bodies supported by different experimental approaches is plotted, binned by whether the site is predicted to undergo methylation or not. The rightmost bars (in gray) reflect an analysis performed on all sites identified by at least one of the five methods.

(E) Agreement between predicted (m6Apred-2) and measured (IP/input) m6A values in human A549 cells (top) and mouse embryonic stem cells (mESCs) (bottom), in both WT cells (left) and cells depleted of methylation components, as indicated (right). Spearman correlations and p values are shown.

(F) Distribution of PBSSs between predicted and measured (A549 cells) m6A levels on the basis of m6Apred-1 (white) and m6Apred-2 (purple).

(G) Predicted and measured m6A levels across five human genes. Top panels display the IP and input signals, and bottom panels display the m6Apred-2-based prediction along the gene. The per-base correlation between predicted and measured values is shown at the top of each panel.

measurements, now also in an intron-harboring context ($R_s = 0.81$) (Figure 3A, bottom). Experimentally measured m6A profiles in mNol12 and mCoa3 changed only mildly between the intron-harboring and lacking constructs, consistent with only mild differences in predicted profiles, given that they were each cloned with only a single intron (Figures S3B and S3C). To validate this model more broadly, we selected 33 intron-harboring human genes, predicted to have different m6A-profiles in the presence of introns (on the basis of m6Apred-2) in comparison to the absence of introns (on the basis of m6Apred-1). We then overexpressed cDNAs encoding each of these genes and measured m6A profiles via m6A-seq2. As anticipated, we found that the (intron-less) cDNA m6A profiles correlated well with m6Apred-1 predictions but poorly with m6Apred-2 predictions. In contrast, the m6A profiles of genomically encoded counterparts were well predicted by m6Apred-2 but poorly with m6Apred-1 (Figures 3B, 3C, and S3D). The same (exonic) sequence thus gets methylated in a differential—and predictable—manner, depending on the presence and whereabouts of introns.

Application of m6APred-2 to 20,102 human gene-models yielded 262,326 predicted methylation sites, with a mean of ~ 13 predicted sites per gene. These sites were distributed over 76,599 predicted “peaks” (whereby each peak was defined as a consecutive stretch of bases with a predicted methylation signal >0). An average peak comprised 3.4 methylated sites and spanned 373 nt. We obtained similar results across 20,954 mouse genes, where an average of 12.8 sites per gene was distributed across 68,893 peaks.

To evaluate the performance of this model, we assessed its ability to capture m6A features at three different resolutions: individual m6A sites, m6A levels within and between genes, and meta-gene features. To validate the ability of m6Apred-2 to accurately detect individual m6A sites, we sought to investigate what fraction of the predicted sites could be confirmed on the basis of experimental data. We compiled an assembly of high-confidence m6A sites detected via distinct experimental single-nucleotide resolution methods (miCLIP,³⁵ SAC-seq,³⁹ miCLIP2,⁴⁰ DART-seq,³⁷ and GLORI⁴¹). We then assessed the overlap between the predicted methylation status and the experimental measurements across 7,268 genes that had been pre-filtered based on expression levels. While all sets of measurements provided substantial support to predictions by our model (Figure 3D), the most compelling results were observed via the recently established GLORI approach, which experimentally validates $\sim 62\%$ of all sites that we predict to undergo methylation, whereas only 6.3% of sites that we predict not to undergo methylation are experimentally supported by the GLORI dataset. Combining all datasets, 71% of the predicted methylated sites were experimentally validated, in comparison to 12% of the predicted negative ones (Figure 3D), lending considerable support to the predictive power of m6Apred-2.

Next, we explored the ability of the model to predict diversity in methylation *between* genes. We observed a striking correlation ($R_s = 0.67$) between experimentally measured m6A levels in A549 cells³⁴ and mean m6Apred-2 predictions (Figure 3E, top left). Importantly, this correlation coefficient dropped substantially ($R_s = 0.17$) when predicted values were compared against

m6A measurements in A549 cells which had been pre-treated with small interfering RNAs (siRNAs) targeting WTAP (Figure 3E, top right), a critical member of the methyltransferase complex.³⁴ We made essentially identical observations in mouse embryonic stem cells, where we observed excellent agreement between predicted methylation densities and experimentally measured counterparts ($R_s = 0.71$) (Figure 3E, bottom left), which were nearly entirely abolished in METTL3 knockout cells ($R_s = 0.1$) (Figure 3E, bottom right). Consistent results were observed in an analysis of additional human and mouse cell lines (Figure S3E). Thus, roughly 45%–50% of the variability in experimentally measured m6A levels at the gene levels are captured by our model.

m6Apred-2 also performed well in *in silico* reconstructing experimental m6A distribution *within* genes, with genes displaying remarkably high similarity scores between measured and predicted values (Figure 3F). Roughly 15% of the genes displayed excellent similarity scores ($R > 0.8$) across gene bodies—in such cases, measured m6A profiles are nearly perfectly recapitulated using the simple, above-defined model (Figure 3F). Another $\sim 26\%$ of the cases displayed correlations between 0.6 and 0.8, and $\sim 22\%$ displayed correlations ranging from 0.4–0.6. Examples for genes displaying varying similarity scores are displayed in Figure 3G. Median similarity scores in an intron-containing context were 0.54, marking a dramatic improvement over m6Apred-1 predictions that achieved a median score of 0.21 (Figure 2B). Genes with lower methylation levels generally showed substantially poorer similarity scores (Figures 3F and S4A), which is anticipated given that in low-methylated genes the relative levels of signal (true methylation) to background (non-specific binding) are low. We also found that m6Apred-2 tended to underestimate m6A signal in 5' UTR regions (Figures S4B and S4C), likely due to a substantial portion of m6A enrichment in the 5' UTR not reflecting m6A, but instead m6Am, installed by a different machinery at non-DRACH related sites.^{34,42–44}

Finally, at the metagene level, we found that the predicted m6A profiles recapitulated the relative depletion of m6A from highly expressed genes (Figure S4D), reflecting the generally more compact structures of highly expressed genes comprising shorter exons and shorter 3' UTRs.⁴⁵ An additional hallmark of m6A distribution, the peak in the last exon, was also well captured by m6Apred-2 (Figure S5A). We noted, however, that the sharp decline in the last exon, which is typically observed in experimentally derived m6A metagene plots (Figure S5A, left), was only partially predicted by m6Apred-2. We hypothesized that methylation might be occluded not only from the vicinity of splice junctions but also from polyadenylation sites, potentially due to masking by the megadalton-polyadenylation and transcription-termination machineries. To explore this hypothesis, we generated a series of constructs where the m6A site was embedded at varying distances from the polyadenylation site ranging from 25 to 200 nt. We found that reducing the distance to the polyadenylation site led to continuously decreasing methylation levels (Figure S5B). We also noted that 3' annotations tended to considerably overestimate 3' UTRs lengths, likely because cell-type agnostic annotations are often based on the longest isoform; such overestimates of 3' lengths give rise to

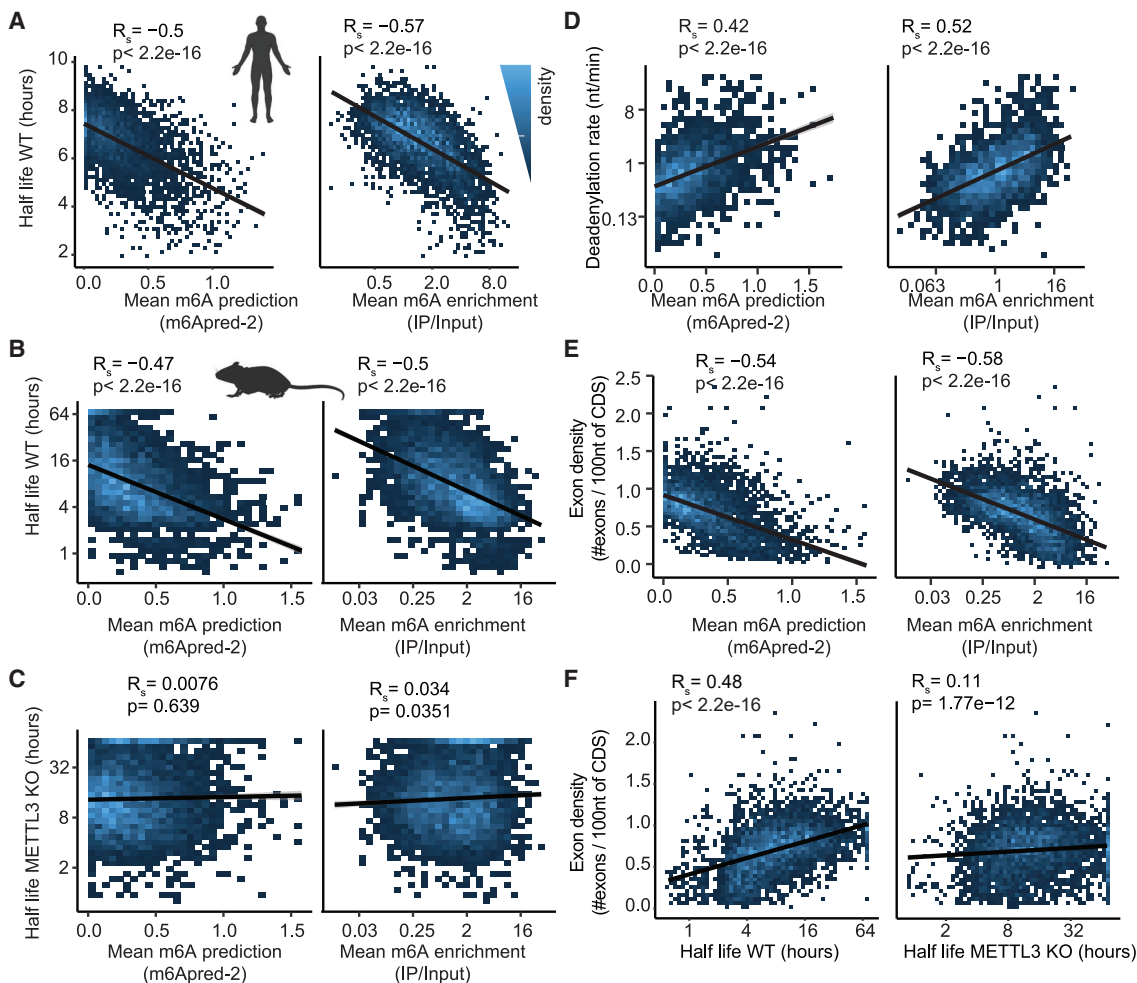


Figure 4. Exon-intron architecture drives mRNA stability through m6A

(A) (Left) correlation between predicted m6A levels (m6Apred-2) and log-transformed mRNA stability rates in human cells. mRNA stability rates in MCF cells were obtained from Schueler et al. (2014).⁴⁸ (right). Correlation between measured m6A levels in A549 cells and mRNA stability. Spearman correlation coefficients and p-values are indicated on each panel of this figure.

(B) Plots as in (A), in mESCs on the basis of predictions and measurements in mESCs.

(C) Corresponding plots of predicted and measured m6A levels in mESCs against decay rates measured in METTL3 KO mESCs.

(D) Correlation between predicted and measured m6A levels in mESCs against deadenylation rates measured in mouse 3T3 cells.

(E) Correlation of exon density with predicted (left) and measured (right) m6A levels in mESCs.

(F) Correlation of exon density with decay rate in WT and METTL3 KO mESCs. Mouse half-life values were capped at 72 h.

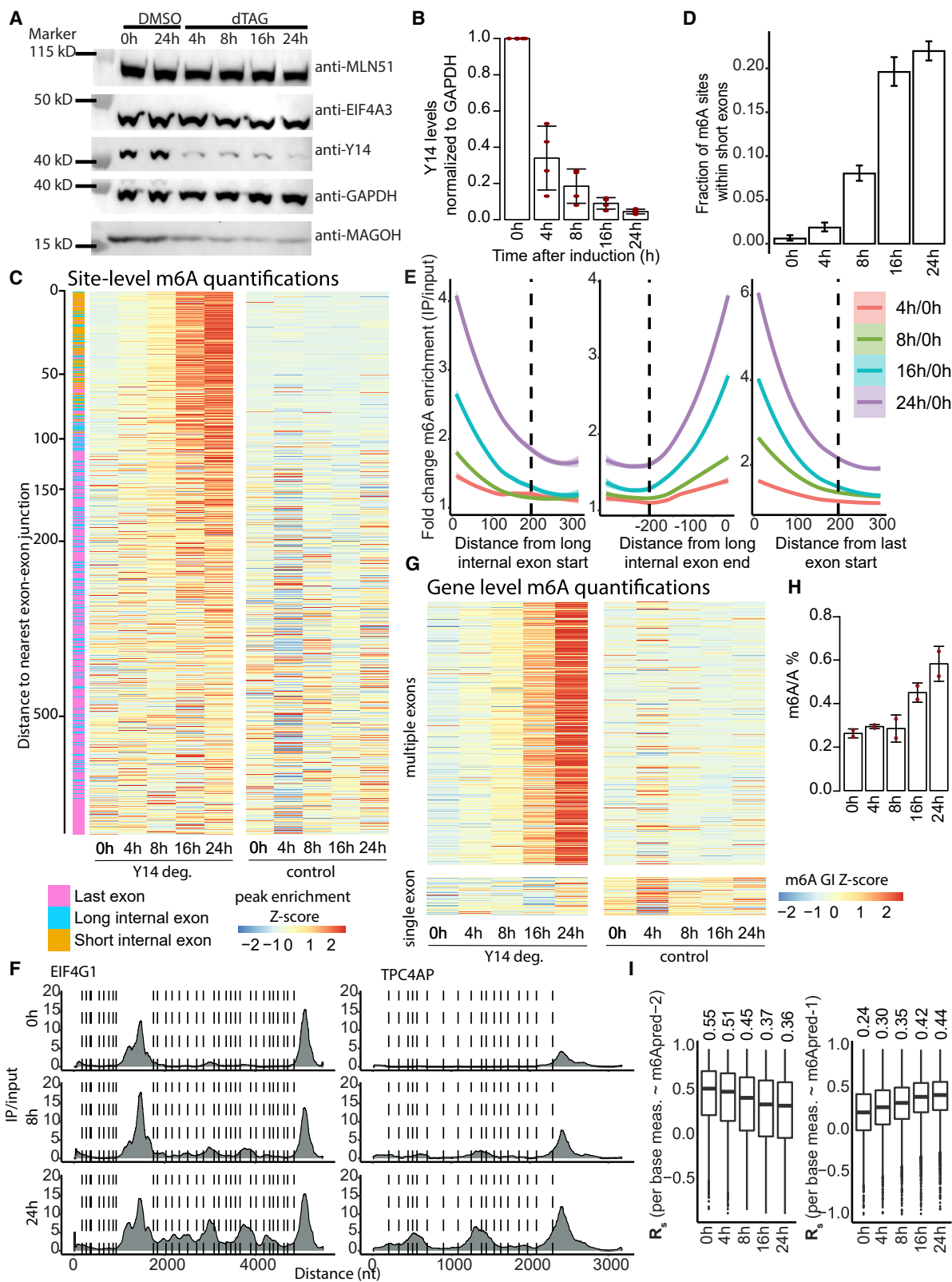
predicted methylations in deep 3' UTR regions that do not occur in practice (Figure S5C). To assess whether the rapid decline of the peak at the terminal exon could be explained by these two factors, we first reannotated gene ends based on the input data (STAR Methods) and then updated m6Apred-2 to not allow methylations to occur at motifs adjacent to the polyadenylation site. This was sufficient to predict both the last exon peak and the rapid decline (Figure S5A, right), reminiscent of the one observed experimentally (Figure S5A, left). These findings suggest that while the peak in the last exon is due to m6A exclusion from splice junctions, the decline may partially be a consequence of exclusion of m6A also from polyadenylation sites.

Collectively, these findings establish that transcriptome-wide m6A topologies in humans and mice are to a large extent shaped

by exclusion, primarily from splice-junction proximal regions and potentially also from the vicinity of polyadenylation sites.

Exon-intron architecture dictates RNA stability via m6A

We next sought to explore the extent to which m6Apred-2 was predictive of mRNA stability. We found both in humans and in mice that predicted m6A levels correlated strongly with RNA stability ($R_s = -0.5$ and -0.47 , respectively), close to the experimentally measured counterparts ($R_s = -0.57$ and -0.5 , respectively) (Figures 4A and 4B). These correlations with half-life between either the predicted m6A level or the experimentally measured one are both abolished in METTL3 knockout (KO) mESCs (Figure 4C). To ensure the robustness of these associations, we obtained mRNA stability measurements from 34



(legend on next page)

different studies in humans and mice (assembled in Agarwal and Kelley [2022]¹⁹), revealing consistent negative correlations between half-lives and both predicted and measured m6A levels (Figures S5D and S5E). Further supporting the ability of our model to capture mRNA stability, we found that mRNA deadenylation rates, available in mouse 3T3 cells,⁴⁶ correlate well with predicted m6A levels ($R_s = 0.42$), close to levels achieved with measured ones ($R_s = 0.52$) (Figure 4D), consistent with findings that binding of m6A by YTH-domain harboring proteins results in deadenylase recruitment.⁴⁷

The strong dependency of m6A on exon-intron architecture prompted us to explore whether m6A was the missing link connecting exon-intron architecture and mRNA stability.^{16–19} We found that exon density correlates strongly with both measured ($R_s = -0.58$) and predicted ($R_s = -0.54$) m6A levels (Figure 4E), suggesting that exon density may be an indirect metric capturing m6A derived signal. To causally dissect this correlation, we explored the relationship between exon density and mRNA stability in WT and METTL3 KO mESCs. We recapitulated a strong correlation between mRNA half-life and exon density in WT cells ($R_s = 0.48$). However, this correlation was nearly entirely abolished in METTL3 KO mESCs ($R_s = 0.11$) (Figure 4F). To gain further support for these findings, we measured mRNA stability in HEK293T cells acutely depleted of m6A using STM2457,⁴⁹ an METTL3 inhibitor, and in mock-treated controls (Figure S6A) and observed reduced association between m6A and mRNA stability (Figure S6B) as well as between mRNA stability and exon density upon METTL3 inhibition (Figure S6C). These findings thus suggest that m6A—by virtue of being depleted from exon-rich regions—serves as the mechanism connecting exon-intron architecture to mRNA decay.

Depletion of m6A from splice junctions is mediated via the EJC

Given the tight association of the EJC at exon-exon boundaries, we hypothesized that this complex might mediate loss of m6A

from junction-proximal consensus motifs. Under this model, elimination of the EJC should lead to accumulation of m6A at eligible motifs within otherwise excluded zones. To investigate this possibility, we introduced a dTAG degron⁵⁰ downstream of Y14, a core EJC component, leading to efficient depletion over a 24-h time course (Figures 5A and 5B). Remarkably, application of m6A-seq2 followed by peak-calling to samples harvested along this time course revealed a progressive and dramatic accumulation of m6A within—but not outside—of exclusion zones. Specifically, when we ordered all identified m6A peaks based on distance from the splice junction, a pronounced induction of m6A levels with Y14 depletion was observed up to a distance of ~200 nt, whereas few changes occurred in m6A intensities for sites more distal from splice junctions (Figures 5C, 5E, and 5F). Consistently, the fraction of peaks within short exons grew substantially over the course of Y14 depletion, with only 0.59% of the called peaks residing within short exons at 0 h in comparison to 21.89% at 24 h following depletion (Figure 5D). Thus, the depletion of m6A from short exons and from junction-proximal regions is reversed with progressive EJC removal, consistent with a model that the EJC prevents their methylation. Furthermore, an analysis of gene-level m6A revealed a pronounced increase in m6A levels across multi-exon genes, and yet—critically—not in single-exon genes, which should not be affected by EJC loss (Figures 5G and S6D). Finally, we were also able to confirm a dramatic induction of bulk m6A levels following EJC loss via mass spectrometry of digested mRNA-derived nucleic acids (Figure 5H).

If the EJC prevents methylation from occurring at junction-proximal sequences, this gives rise to two predictions. First, the ability to predict m6A landscapes *in silico* on the basis of m6Apred-2—which takes into account exon-intron architecture—should continuously decrease with progressive Y14 depletion. Second, the ability to predict m6A landscapes *in silico* on the basis of m6Apred-1, which only takes into account motif availability but not exon-intron architecture, should continuously

Figure 5. Inducible target-specific depletion of EJC member Y14 leads to increased methylation in multi-exonic genes in short exons

- (A) Representative Western blot images of Y14 degron and control DMSO-treated time points, with antibodies against different EJC members and control GAPDH. Uncut gels are presented in Figure S6G.
- (B) Quantification of Western blot band intensities of Y14 normalized to GAPDH in the Y14 degron time points, based on four biological replicates. Red marks individual measurement data points, error bars indicate standard deviation of the mean.
- (C) Heatmap of row-scaled m6A site scores of all Y14 degradation and control samples analyzed for unique m6A-sites that were previously detected by *de novo* m6A peak calling (see STAR Methods) based on all Y14 degradation samples (0 h, 4 h, 8 h, 16 h, and 24 h). m6A-sites were ordered by the distance to the closest exon-exon junction (distances indicated in black, left) and labeled by the type of exon (small internal exon, <200 bases; long internal exon; >200 bases; and last exon).
- (D) Bar plot depicting the ratio of m6A sites that were depicted in small internal exons compared to any other type of exon. Error bars show the 95% confidence interval of the test of equal proportions.
- (E) Meta fold-change m6A-IP/input of timepoints after the induction of Y14 degradation (4 h, 8 h, 16 h, and 24 h) compared to timepoint 0 h. Analysis was performed for 300 bases of the 5' beginning (left), 300 bases before the 3' end (center) of long internal exons (>600 bases), and the 5' beginning of last exons (right). Calculated fold-changes are based on the median m6A-IP/input score for 10-nt-long bins per time point.
- (F) Heatmap showing the row-scaled m6A gene index (m6A-GIs) of all the samples of the Y14 degradation dataset for genes annotated with >1 exon (multiple exons, top) and single-exon genes (bottom).
- (G) m6A IP/input coverage (y axis) per base in transcript space (x axis) based on three samples of the Y14 degradation dataset (0 h, 8 h, and 24 h) for two representative genes *EIF4G1* (left) and *TPC4AP* (right). Dashed lines mark exon-exon boundaries.
- (H) m6A/A percentage of the indicated time points of the Y14 degron samples, measured by LC-MS/MS. Red marks individual measurement data points, error bars indicate standard deviation of the mean.
- (I) (Left) distribution of per-base correlations between m6Apred-2 predictions of m6A levels and experimentally measured counterparts (capturing the ability of m6Apred-2 to predict m6A variability *within* genes), plotted at indicated time points following Y14 depletion. (Right) as in the left, but on the basis of m6Apred-1 predictions. Boxplots correspond to the median, Q1, and Q3; whiskers mark Q1 – 1.5 IQR and Q3 + 1.5 IQR.

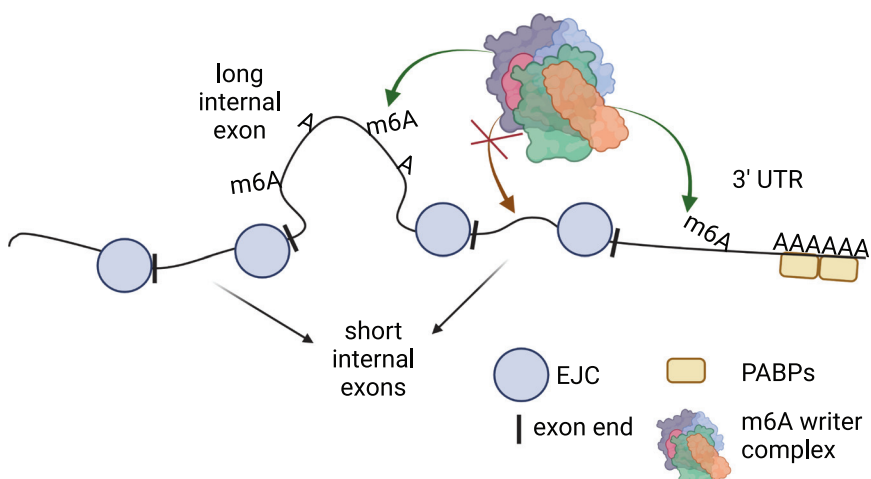


Figure 6. Model proposing the physical exclusion of methylation marks near splice junctions by the EJC
PABP: poly(A) binding protein. See also Discussion.

increase with progressive depletion. Both trends were evident based on analyses capturing m6A variability both within (Figure 5*I*) and between genes (Figure S6*E*). Thus, upon depletion of a critical EJC component, m6A landscapes gradually cease to be governed by proximity to splice junctions, leading to the predictable emergence of m6A sites within m6A exclusion zones.

Collectively, these findings strongly implicate the EJC in restricting methylation near splice sites, serving as the link connecting exon-intron architecture to m6A deposition and thereby to mRNA stability.

DISCUSSION

Here we propose a model for how specificity in m6A deposition is achieved. We propose that m6A deposition is dictated by sequence motifs and exon-intron architecture, and we demonstrate that the depletion from splice-site proximity is mediated via the EJC. In unraveling the link between m6A and exon-intron architecture, we also identify a mechanism linking exon-intron architecture to mRNA stability. Our findings suggest that deposition of m6A is radically different from tRNA and rRNA modifications: while the latter are selectively installed at specific positions, m6A is installed in a non-selective manner and is governed by exclusion. Rather than being present on only a handful of sites per gene, our model predicts that m6A is installed at hundreds of thousands of sites transcriptome-wide, with an average of ~13 m6A sites per gene, which is consistent with most recent measurements of m6A on the basis of GLORI, reporting an average of ~10 sites per gene.⁴¹ Our findings have important bearings on the biogenesis, regulation, and function of m6A; on our understanding of the determinants and regulation of mRNA stability; and on our understanding of a new critical role played by the EJC. Our findings further offer an attractive lens through which to re-examine additional contexts in which the cytoplasmic fate of an mRNA (e.g., localization, translation) were found to be associated with nuclear splicing.^{21–26,51,52}

How does the EJC prevent methylation from occurring at splice-site proximal consensus motifs? One possibility is that EJCs physically occlude m6A consensus motifs, thereby pre-

venting access of the megadalton RNA methylation machinery⁵³ (Figure 6). The 8-nt footprint of EJCs⁵⁴ is insufficient to account for the depletion across a 200-bp window. This large exclusion zone most likely results from tight association of EJCs with other RBPs including members of the SR family^{27,55} with a footprint of 30–150 nt.²⁷ In this scenario, methylation occurs following EJC deposition as a consequence of splicing.²⁸ This is consistent with studies finding m6A to be strongly depleted from introns.^{9,14,56} We do note, however, that m6A was found to be present at near steady-state levels already on chromatin-associated RNA¹⁴ and was reported by one study on nascent RNA⁵⁷ and in another in introns,⁵⁸ albeit at low levels, which would be inconsistent with the posited model.

Our findings have widespread implications on the regulation of m6A and of mRNA stability. The majority of exons are constitutively spliced most of the time. As such, mechanisms tied to splicing are similarly expected to be constitutive, to a considerable extent. This is consistent with the relative robustness of m6A profiles across different cell and tissue types^{34,59} as well as with recent findings that mRNA stability is also highly correlated across diverse cell types.¹⁹ Nonetheless, exon-intron architecture can be modulated via different forms of alternative splicing or via alternative polyadenylation, which can alter the proximity of m6A consensus sites to splice junctions, thereby impacting methylation and, in turn, mRNA stability. Alternative polyadenylation events are particularly interesting to consider, as it has been observed in diverse contexts that longer isoforms are less stable. This reduced stability was attributed to abolishment of microRNA binding sites, though this abolishment was shown to only account for a minor portion of this destabilization.^{60,61} Our results offer a fresh interpretation for these observations given that longer 3' UTRs give rise to broad methylation-permissive regions (vertebrate 3' UTR typically lacks introns), which increase the methylation load of a gene and would therefore be predicted to reduce stability.

It is interesting to speculate about the “logic” of coupling mRNA degradation to the absence of splice junctions. One possibility is that such coupling came about in order to inhibit gene expression from retrotransposons. Such elements are pervasive in the human genome, they lack introns, and their expression has the potential to create havoc. Retrotransposons are epigenetically silenced at the transcriptional level via 5mC on DNA—indeed, 5mC is speculated to have evolved as a mechanism for their silencing.^{62,63} m6A, which—similar to m5C—we now find to be installed by default, and which also imposes silencing at the RNA level, may serve as a post-transcriptional

counterpart. This idea resonates with recent literature implicating m6A in the silencing of transposable elements.^{64–68}

Limitations of the study

Our model exhibits a substantial, yet still incomplete, agreement with experimentally measured methylation levels, explaining roughly ~50% of the variability in m6A levels between genes and ~25% of the variability within a median gene. This incomplete agreement is likely attributed to several factors. First, a strength—but also weakness—of our model is its simplicity: it relies on binary, rather than probabilistic, decisions regarding the eligibility of motifs and splice-junction distances. Second, the experimental measurements on which we rely are limited and are subject to biases due to antibody promiscuity^{3,69} and incomplete sensitivity.² Finally, as indicated above, genomic annotations—on which the model heavily relies—are an additional source of error. More quantitative models, based on improved and more quantitative m6A measurements and improved annotations, will allow an updated estimate of the fraction of m6A deposition not accounted for by our findings and potentially allow discovery of additional levels shaping m6A deposition.

Our findings provide a unifying framework, quantitatively and causally connecting exon-intron architecture, the EJC, m6A deposition, and mRNA stability. We anticipate that this study will open up future explorations into the logic of tying mRNA stability to exon-intron architecture and into physiological and pathological contexts in which regulation of EJC deposition, via modulation of splicing, regulates mRNA stability by controlling the deposition of m6A.

STAR★METHODS

Detailed methods are provided in the online version of this paper and include the following:

- KEY RESOURCES TABLE
- RESOURCE AVAILABILITY

- Lead contact
- Materials availability
- Data and code availability

- EXPERIMENTAL MODEL AND SUBJECT DETAILS
- METHOD DETAILS

- Cloning of the short oligo library pool
- Design of the short oligo library pool
- Cloning of the long, splicing oligo library pool
- Cloning of the *Coa3*, *No12*, and *Calm3* plasmids
- Cloning of cDNA constructs
- Cell culture and transfactions
- Preparation and validation of Y14-HA-dTAG HEK293T cell
- dTAG time-course treatment
- LC-MS/MS for quantification of m6A/A
- SCARLET analyses for quantification of m6A/A
- RNA extraction, m6A IP, and library preparation
- Datasets analyzed in this study
- Alignment and calculation of IP/input enrichment scores
- Implementation of m6Apred-1 and m6Apred-2 models

- Analysis of METTL3 inhibitor RNA degradation timepoints
- Analysis of Y14 degron timepoints m6A IP data
- *De novo* m6A peak calling

- QUANTIFICATION AND STATISTICAL ANALYSIS

SUPPLEMENTAL INFORMATION

Supplemental information can be found online at <https://doi.org/10.1016/j.molcel.2022.12.026>.

ACKNOWLEDGMENTS

We are grateful to Ghil Jona (Bacteriology & Genomic Repository Unit, Weizmann Institute of Science) for sharing dozens of plasmids from the ORFeome collection, to Joe Georgeson for conceiving the cDNA overexpression experiment, and to Quentin Alasseur for adapting the dTAG degron strategy. S.S. is funded by the Israel Science Foundation (913/21) and by the European Research Council (ERC) under the European Union's Horizon 2020 research and innovation program (grant no. 714023 and 101000970). S.S. is the incumbent of the Robert Edward and Roselyn Rich Manson Career Development Chair in Perpetuity. H.L.H. was supported by the Agence Nationale de la Recherche (ANR-17-CE12-0021 and ANR-21-CE12-0041), by Fondation pour la Recherche Médicale (FRM EQU202003010226), and by continuous financial support from the Centre National de la Recherche Scientifique, the École Normale Supérieure, and the Institut National de la Santé et de la Recherche Médicale, France. W.R. was supported by the Austrian Science Fund (F 8013). A.U. is grateful to the Azrieli Foundation for the award of an Azrieli Fellowship.

AUTHOR CONTRIBUTIONS

B.S., A.U., and S.S. conceived the project. B.S., A.U., and R.N performed most of the experiments. A.U., D.D., and S.S. performed the computational analyses. S.S. implemented the m6A prediction models. S.S. wrote the manuscript with input from all authors. O.S.K., C.B., I.B., and H.L.H. performed the Y14 degron experiments. U.T. and W.R. acquired the SCARLET measurements. A.B. performed the mass spectrometry experiments.

DECLARATION OF INTERESTS

S.S. is a member of the scientific advisory board of 858 Therapeutics. S.S. is currently spending a sabbatical year at Genentech, Inc.

Received: May 26, 2022

Revised: November 4, 2022

Accepted: December 21, 2022

Published: January 3, 2023

REFERENCES

1. Perry, R.P., Kelley, D.E., Friderici, K., and Rottman, F. (1975). The methylated constituents of L cell messenger RNA: evidence for an unusual cluster at the 5' terminus. *Cell* **4**, 387–394.
2. Garcia-Campos, M.A., Edelheit, S., Toth, U., Safra, M., Shachar, R., Viukov, S., Winkler, R., Nir, R., Lasman, L., Brandis, A., et al. (2019). Deciphering the “m6A Code” via antibody-independent quantitative profiling. *Cell* **178**, 731–747.e16.
3. Schwartz, S., Agarwala, S.D., Mumbach, M.R., Jovanovic, M., Mertins, P., Shishkin, A., Tabach, Y., Mikkelsen, T.S., Satija, R., Ruvkun, G., et al. (2013). High-resolution mapping reveals a conserved, widespread, dynamic mRNA methylation program in yeast meiosis. *Cell* **155**, 1409–1421.
4. Dominissini, D., Moshitch-Moshkovitz, S., Schwartz, S., Salmon-Divon, M., Ungar, L., Osenberg, S., Cesarkas, K., Jacob-Hirsch, J., Amariglio, N., Kupiec, M., et al. (2012). Topology of the human and mouse m6A RNA methylomes revealed by m6A-seq. *Nature* **485**, 201–206.

5. Meyer, K.D., Saletoye, Y., Zumbo, P., Elemento, O., Mason, C.E., and Jaffrey, S.R. (2012). Comprehensive analysis of mRNA methylation reveals enrichment in 3' UTRs and near Stop codons. *Cell* 149, 1635–1646.
6. Ke, S., Alemu, E.A., Mertens, C., Gantman, E.C., Fak, J.J., Mele, A., Haripal, B., Zucker-Scharff, I., Moore, M.J., Park, C.Y., et al. (2015). A majority of m6A residues are in the last exons, allowing the potential for 3' UTR regulation. *Genes Dev.* 29, 2037–2053.
7. Xiao, W., Adhikari, S., Dahal, U., Chen, Y.-S., Hao, Y.-J., Sun, B.-F., Sun, H.-Y., Li, A., Ping, X.-L., Lai, W.-Y., et al. (2016). Nuclear m(6)A reader YTHDC1 regulates mRNA splicing. *Mol. Cell* 61, 507–519. <https://doi.org/10.1016/j.molcel.2016.01.012>.
8. Lence, T., Akhtar, J., Bayer, M., Schmid, K., Spindler, L., Ho, C.H., Kreim, N., Andrade-Navarro, M.A., Poeck, B., Helm, M., and Roignant, J.Y. (2016). m6A modulates neuronal functions and sex determination in Drosophila. *Nature* 540, 242–247. <https://doi.org/10.1038/nature20568>.
9. Wei, G., Almeida, M., Pintacuda, G., and Coker, H. (2021). Acute depletion of METTL3 implicates N6-methyladenosine in alternative intron/exon inclusion in the nascent transcriptome. *Genome* 31, 1395–1408.
10. Yang, X., Liu, Q.-L., Xu, W., Zhang, Y.-C., Yang, Y., Ju, L.-F., Chen, J., Chen, Y.-S., Li, K., Ren, J., et al. (2019). m6A promotes R-loop formation to facilitate transcription termination. *Cell Res.* 29, 1035–1038. <https://doi.org/10.1038/s41422-019-0235-7>.
11. Abakir, A., Giles, T.C., Cristini, A., Foster, J.M., Dai, N., Starczak, M., Rubio-Roldan, A., Li, M., Eleftheriou, M., Crutchley, J., et al. (2020). N 6 -methyladenosine regulates the stability of RNA:DNA hybrids in human cells. *Nat. Genet.* 52, 48–55.
12. Wang, X., Lu, Z., Gomez, A., Hon, G.C., Yue, Y., Han, D., Fu, Y., Parisien, M., Dai, Q., Jia, G., et al. (2014). N6-methyladenosine-dependent regulation of messenger RNA stability. *Nature* 505, 117–120.
13. Zaccara, S., and Jaffrey, S.R. (2020). A unified model for the function of YTHDF Proteins in regulating m6A-modified mRNA. *Cell* 181, 1582–1595.e18.
14. Ke, S., Pandya-Jones, A., Saito, Y., Fak, J.J., Vågbø, C.B., Geula, S., Hanna, J.H., Black, D.L., Darnell, J.E., Jr., and Darnell, R.B. (2017). m6A mRNA modifications are deposited in nascent pre-mRNA and are not required for splicing but do specify cytoplasmic turnover. *Genes Dev.* 31, 990–1006.
15. Diers, D., Garcia-Campos, M.A., Uzonyi, A., Safra, M., Edelheit, S., Rossi, A., Sideri, T., Varier, R.A., Brandis, A., Stelzer, Y., et al. (2021). Multiplexed profiling facilitates robust m6A quantification at site, gene and sample resolution. *Nat. Methods* 18, 1060–1067.
16. Spies, N., Burge, C.B., and Bartel, D.P. (2013). 3' UTR-isoform choice has limited influence on the stability and translational efficiency of most mRNAs in mouse fibroblasts. *Genome Res.* 23, 2078–2090. <https://doi.org/10.1101/gr.156919.113>.
17. Agarwal, V., and Shendure, J. (2020). Predicting mRNA abundance directly from genomic sequence using deep convolutional neural networks. *Cell Rep.* 31, 107663.
18. Sharova, L.V., Sharov, A.A., Nedorezov, T., Piao, Y., Shaik, N., and Ko, M.S.H. (2009). Database for mRNA half-life of 19 977 genes obtained by DNA microarray analysis of pluripotent and differentiating mouse embryonic stem cells. *DNA Res.* 16, 45–58.
19. Agarwal, V., and Kelley, D.R. (2022). The genetic and biochemical determinants of mRNA degradation rates in mammals. *Genome Biology* 23, 245. <https://doi.org/10.1101/2022.03.18.484474>.
20. Clark, M.B., Johnston, R.L., Inostroza-Ponta, M., Fox, A.H., Fortini, E., Moscato, P., Dinger, M.E., and Mattick, J.S. (2012). Genome-wide analysis of long noncoding RNA stability. *Genome Res.* 22, 885–898.
21. Le Hir, H., Nott, A., and Moore, M.J. (2003). How introns influence and enhance eukaryotic gene expression. *Trends Biochem. Sci.* 28, 215–220.
22. Buchman, A.R., and Berg, P. (1988). Comparison of intron-dependent and intron-independent gene expression. *Mol. Cell Biol.* 8, 4395–4405.
23. Proudfoot, N.J., Furger, A., and Dye, M.J. (2002). Integrating mRNA processing with transcription. *Cell* 108, 501–512.
24. Luo, M.J., and Reed, R. (1999). Splicing is required for rapid and efficient mRNA export in metazoans. *Proc. Natl. Acad. Sci. USA* 96, 14937–14942.
25. Dwyer, K., Agarwal, N., Pile, L., and Ansari, A. (2021). Gene architecture facilitates intron-mediated enhancement of transcription. *Front. Mol. Biosci.* 8, 669004.
26. Matsumoto, K., Wassarman, K.M., and Wolffe, A.P. (1998). Nuclear history of a pre-mRNA determines the translational activity of cytoplasmic mRNA. *EMBO J.* 17, 2107–2121. <https://doi.org/10.1093/emboj/17.7.2107>.
27. Singh, G., Kucukural, A., Cenik, C., Leszyk, J.D., Shaffer, S.A., Weng, Z., and Moore, M.J. (2012). The cellular EJC interactome reveals higher-order mRNP structure and an EJC-SR protein nexus. *Cell* 151, 915–916.
28. Le Hir, H., Saulière, J., and Wang, Z. (2016). The exon junction complex as a node of post-transcriptional networks. *Nat. Rev. Mol. Cell Biol.* 17, 41–54.
29. Adivarahan, S., Livingston, N., Nicholson, B., Rahman, S., Wu, B., Rissland, O.S., and Zenklusen, D. (2018). Spatial organization of single mRNPs at different stages of the gene expression pathway. *Mol. Cell* 72, 727–738.e5.
30. Metkar, M., Ozadam, H., Lajoie, B.R., Imakaev, M., Mirny, L.A., Dekker, J., and Moore, M.J. (2018). Higher-order organization principles of pre-translational mRNPs. *Mol. Cell* 72, 715–726.e3.
31. Khong, A., and Parker, R. (2018). mRNP architecture in translating and stress conditions reveals an ordered pathway of mRNP compaction. *J. Cell Biol.* 217, 4124–4140.
32. Woodward, L.A., Mabin, J.W., Gangras, P., and Singh, G. (2017). The exon junction complex: a lifelong guardian of mRNA fate. *WIREs RNA* 8. <https://doi.org/10.1002/wrna.1411>.
33. Gehring, N.H., Lamprinaki, S., Hentze, M.W., and Kulozik, A.E. (2009). The hierarchy of exon-junction complex assembly by the spliceosome explains key features of mammalian nonsense-mediated mRNA decay. *PLoS Biol.* 7, e1000120.
34. Schwartz, S., Mumbach, M.R., Jovanovic, M., Wang, T., Maciag, K., Bushkin, G.G., Mertins, P., Ter-Ovanesyan, D., Habib, N., Cacchiarelli, D., et al. (2014). Perturbation of m6A writers reveals two distinct classes of mRNA methylation at internal and 5' sites. *Cell Rep.* 8, 284–296.
35. Chen, K., Wei, Z., Zhang, Q., Wu, X., Rong, R., Lu, Z., Su, J., de Magalhães, J.P., Rigden, D.J., and Meng, J. (2019). WHISTLE: a high-accuracy map of the human N6-methyladenosine (m6A) epitranscriptome predicted using a machine learning approach. *Nucleic Acids Res.* 47, e41. <https://doi.org/10.1093/nar/gkz074>.
36. Linder, B., Grozhik, A.V., Olarerin-George, A.O., Meydan, C., Mason, C.E., and Jaffrey, S.R. (2015). Single-nucleotide-resolution mapping of m6A and m6Am throughout the transcriptome. *Nat. Methods* 12, 767–772. <https://doi.org/10.1038/nmeth.3453>.
37. Tegowski, M., Flamand, M.N., and Meyer, K.D. (2022). scDART-seq reveals distinct m6A signatures and mRNA methylation heterogeneity in single cells. *Mol. Cell* 82, 868–878.e10. <https://doi.org/10.1016/j.molcel.2021.12.038>.
38. Liu, N., Parisien, M., Dai, Q., Zheng, G., He, C., and Pan, T. (2013). Probing N6-methyladenosine RNA modification status at single nucleotide resolution in mRNA and long noncoding RNA. *RNA* 19, 1848–1856.
39. Hu, L., Liu, S., Peng, Y., Ge, R., Su, R., Senevirathne, C., Harada, B.T., Dai, Q., Wei, J., Zhang, L., et al. (2022). m6A RNA modifications are measured at single-base resolution across the mammalian transcriptome. *Nat. Biotechnol.* 40, 1210–1219.
40. Körtel, N., Rücklé, C., Zhou, Y., Busch, A., Hoch-Kraft, P., Sutandy, F.X.R., Haase, J., Pradhan, M., Musheev, M., Ostareck, D., et al. (2021). Deep and accurate detection of m6A RNA modifications using miCLIP2 and m6Aboost machine learning. *Nucleic Acids Res.* 49, e92.
41. Liu, C., Sun, H., Yi, Y., Shen, W., Li, K., Xiao, Y., Li, F., Li, Y., Hou, Y., Lu, B., et al. (2022). Absolute quantification of single-base m6A methylation in the

- mammalian transcriptome using GLORI. *Nat. Biotechnol.* <https://doi.org/10.1038/s41587-022-01487-9>.
42. Mauer, J., Luo, X., Blanjoie, A., Jiao, X., Grozhik, A.V., Patil, D.P., Linder, B., Pickering, B.F., Vasseur, J.-J., Chen, Q., et al. (2017). Reversible methylation of m6Am in the 5' cap controls mRNA stability. *Nature* **541**, 371–375.
 43. Akichika, S., Hirano, S., Shichino, Y., Suzuki, T., Nishimatsu, H., Ishitani, R., Sugita, A., Hirose, Y., Iwasaki, S., Nureki, O., and Suzuki, T. (2019). Cap-specific terminal N 6-methylation of RNA by an RNA polymerase II-associated methyltransferase. *Science* **363**, eaav0080. <https://doi.org/10.1126/science.aav0080>.
 44. Keith, J.M., Ensinger, M.J., and Moss, B. (1978). HeLa cell RNA (2'-O-methyladenosine-N6-)methyltransferase specific for the capped 5'-end of messenger RNA. *J. Biol. Chem.* **253**, 5033–5039.
 45. Eisenberg, E., and Levanon, E.Y. (2003). Human housekeeping genes are compact. *Trends Genet.* **19**, 362–365.
 46. Eisen, T.J., Eichhorn, S.W., Subtelny, A.O., Lin, K.S., McGeary, S.E., Gupta, S., and Bartel, D.P. (2020). The dynamics of cytoplasmic mRNA metabolism. *Mol. Cell* **77**, 786–799.e10.
 47. Du, H., Zhao, Y., He, J., Zhang, Y., Xi, H., Liu, M., Ma, J., and Wu, L. (2016). YTHDF2 destabilizes m6A-containing RNA through direct recruitment of the CCR4–NOT deadenylase complex. *Nat. Commun.* **7**, 12626–12711.
 48. Schueler, M., Munschauer, M., Gregersen, L.H., Finzel, A., Loewer, A., Chen, W., Landthaler, M., and Dieterich, C. (2014). Differential protein occupancy profiling of the mRNA transcriptome. *Genome Biol.* **15**, R15.
 49. Yankova, E., Blackaby, W., Albertella, M., Rak, J., De Braekeleer, E., Tsagkogeorga, G., Pilka, E.S., Aspris, D., Leggate, D., Hendrick, A.G., et al. (2021). Small-molecule inhibition of METTL3 as a strategy against myeloid leukaemia. *Nature* **593**, 597–601.
 50. Nabet, B., Roberts, J.M., Buckley, D.L., Paultk, J., Dastjerdi, S., Yang, A., Leggett, A.L., Erb, M.A., Lawlor, M.A., Souza, A., et al. (2018). The dTAG system for immediate and target-specific protein degradation. *Nat. Chem. Biol.* **14**, 431–441.
 51. Le Hir, H., Gatfield, D., Izaurralde, E., and Moore, M.J. (2001). The exon-exon junction complex provides a binding platform for factors involved in mRNA export and nonsense-mediated mRNA decay. *EMBO J.* **20**, 4987–4997.
 52. Zuckerman, B., Ron, M., Mikl, M., Segal, E., and Ulitsky, I. (2020). Gene architecture and sequence composition underpin selective dependency of nuclear export of long RNAs on NXF1 and the TREX complex. *Mol. Cell* **79**, 251–267.e6.
 53. Bokar, J.A., Shambaugh, M.E., Polayes, D., Matera, A.G., and Rottman, F.M. (1997). Purification and cDNA cloning of the AdoMet-binding subunit of the human mRNA (N6-adenosine)-methyltransferase. *RNA* **3**, 1233–1247.
 54. Ballut, L., Marchadier, B., Baguet, A., Tomasetto, C., Séraphin, B., and Le Hir, H. (2005). The exon junction core complex is locked onto RNA by inhibition of eIF4AIII ATPase activity. *Nat. Struct. Mol. Biol.* **12**, 861–869.
 55. Saulière, J., Murigneux, V., Wang, Z., Marquet, E., Barbosa, I., Le Tonquéze, O., Audic, Y., Paillard, L., Roest Crollius, H., and Le Hir, H. (2012). CLIP-seq of eIF4AIII reveals transcriptome-wide mapping of the human exon junction complex. *Nat. Struct. Mol. Biol.* **19**, 1124–1131.
 56. Chen-Kiang, S., Nevins, J.R., and Darnell, J.E., Jr. (1979). N-6-methyladenosine in adenovirus type 2 nuclear RNA is conserved in the formation of messenger RNA. *J. Mol. Biol.* **135**, 733–752.
 57. Xu, W., He, C., Kaye, E.G., Li, J., Mu, M., Nelson, G.M., Dong, L., Wang, J., Wu, F., Shi, Y.G., et al. (2022). Dynamic control of chromatin-associated m6A methylation regulates nascent RNA synthesis. *Mol. Cell* **82**, 1156–1168.e7.
 58. Louloupi, A., Ntini, E., Conrad, T., and Ørom, U.A.V. (2018). Transient N-6-methyladenosine transcriptome sequencing reveals a regulatory role of m6A in splicing efficiency. *Cell Rep.* **23**, 3429–3437.
 59. Liu, J., Li, K., Cai, J., Zhang, M., Zhang, X., Xiong, X., Meng, H., Xu, X., Huang, Z., Peng, J., et al. (2020). Landscape and regulation of m6A and m6Am methylome across human and mouse tissues. *Mol. Cell* **77**, 426–440.e6.
 60. Mayr, C., and Bartel, D.P. (2009). Widespread shortening of 3'UTRs by alternative cleavage and polyadenylation activates oncogenes in cancer cells. *Cell* **138**, 673–684.
 61. Sandberg, R., Neilson, J.R., Sarma, A., Sharp, P.A., and Burge, C.B. (2008). Proliferating cells express mRNAs with shortened 3' untranslated regions and fewer microRNA target sites. *Science* **320**, 1643–1647.
 62. Yoder, J.A., Walsh, C.P., and Bestor, T.H. (1997). Cytosine methylation and the ecology of intragenomic parasites. *Trends Genet.* **13**, 335–340.
 63. Deniz, Ö., Frost, J.M., and Branco, M.R. (2019). Regulation of transposable elements by DNA modifications. *Nat. Rev. Genet.* **20**, 417–431.
 64. Chelmicki, T., Roger, E., Teissandier, A., Rucli, S., Dossin, F., Dura, M., Fouassier, C., Lameiras, S., and Bourc'his, D. (2020). m6A RNA methylation regulates the fate of endogenous retroviruses. *Nature* **591**, 312–316. <https://doi.org/10.1101/2020.03.24.2005488>.
 65. Liu, J., Dou, X., Chen, C., Chen, C., Liu, C., Xu, M.M., Zhao, S., Shen, B., Gao, Y., Han, D., and He, C. (2020). N6-methyladenosine of chromosome-associated regulatory RNA regulates chromatin state and transcription. *Science* **367**, 580–586.
 66. Liu, J., Gao, M., He, J., Wu, K., Lin, S., Jin, L., Chen, Y., Liu, H., Shi, J., Wang, X., et al. (2021). The RNA m6A reader YTHDC1 silences retrotransposons and guards ES cell identity. *Nature* **591**, 322–326.
 67. Chen, C., Liu, W., Guo, J., Liu, Y., Liu, X., Liu, J., Dou, X., Le, R., Huang, Y., Li, C., et al. (2021). Nuclear m6A reader YTHDC1 regulates the scaffold function of LINE1 RNA in mouse ESCs and early embryos. *Protein Cell* **12**, 455–474.
 68. Xu, W., Li, J., He, C., Wen, J., Ma, H., Rong, B., Diao, J., Wang, L., Wang, J., Wu, F., et al. (2021). METTL3 regulates heterochromatin in mouse embryonic stem cells. *Nature* **591**, 317–321.
 69. McIntyre, A.B.R., Gokhale, N.S., Cerchietti, L., Jaffrey, S.R., Horner, S.M., and Mason, C.E. Limits in the detection of m6A changes using MeRIP/m6A-seq. *Sci. Rep.* **10**(1), pp.1–15. [10.1101/657130](https://doi.org/10.1101/657130)
 70. Daguenet, E., Baguet, A., Degot, S., Schmidt, U., Alpy, F., Wendling, C., Spiegelhalter, C., Kessler, P., Rio, M.-C., Le Hir, H., et al. (2012). Perispeckles are major assembly sites for the exon junction core complex. *Mol. Biol. Cell* **23**, 1765–1782.
 71. Stelzer, Y., Shivalila, C., Soldner, F., Markoulaki, S., Jaenisch, R., and Jaenisch, R. (2015). Tracing dynamic changes of DNA methylation at single-cell resolution in brief tracing dynamic changes of DNA methylation at single-cell resolution. *Cell* **163**, 218–229.
 72. Uzonyi, A., Nir, R., and Schwartz, S. (2022). Cloning of DNA oligo pools for in vitro expression. *STAR Protoc.* **3**, 101103.
 73. Dobin, A., Davis, C.A., Schlesinger, F., Drenkow, J., Zaleski, C., Jha, S., Batut, P., Chaisson, M., and Gingeras, T.R. (2013). STAR: ultrafast universal RNA-seq aligner. *Bioinformatics* **29**, 15–21.
 74. Quinlan, A.R., and Hall, I.M. (2010). BEDTools: a flexible suite of utilities for comparing genomic features. *Bioinformatics* **26**, 841–842.
 75. Shishkin, A.A., Giannoukos, G., Kucukural, A., Ciulla, D., Busby, M., Surka, C., Chen, J., Bhattacharya, R.P., Rudy, R.F., Patel, M.M., et al. (2015). Simultaneous generation of many RNA-seq libraries in a single reaction. *Nat. Methods* **12**, 323–325.
 76. Hocq, R., Paternina, J., Alasseur, Q., Genovesio, A., and Le Hir, H. (2018). Monitored eCLIP: high accuracy mapping of RNA-protein interactions. *Nucleic Acids Res.* **46**, 11553–11565.
 77. Grosjean, H., Droogmans, L., Roovers, M., and Keith, G. (2007). Detection of enzymatic activity of transfer RNA modification enzymes using radiolabeled tRNA substrates. *Methods Enzymol.* **425**, 55–101.

STAR★METHODS

KEY RESOURCES TABLE

REAGENT or RESOURCE	SOURCE	IDENTIFIER
Antibodies		
α -M6A	Synaptic systems	Cat# 202 003, RRID:AB_2279214
α -M6A	Cell Signaling	Cat# 56593, RRID:AB_2799515
Y14 antibody	Santa Cruz Biotechnology	Cat# sc-32312, RRID:AB_2178827
HA antibody	Sigma-Aldrich	Cat#H6908, RRID:AB_260070
α -eIF4A3	Daguenet et al. ⁷⁰	N/A
α -MLN51	Daguenet et al. ⁷⁰	N/A
α -MAGOH	kind gift from E. Izaurrealde, Max Planck Institute for Developmental Biology	N/A
Anti-Mouse HRP conjugate	PROMEGA	Cat#W402B, RRID:AB_430834
Anti-Rabbit HRP conjugate	PROMEGA	Cat#W401B, RRID:AB_430833
α -GAPDH	Cell Signaling	Cat# 2118S, RRID:AB_561053
Chemicals, peptides, and recombinant proteins		
high-grade fetal bovine serum	Biological Industries	Cat#04-001-1A
Kapa HiFi DNA polymerase	Roche	Cat# KK2602
dTAG13	Sigma-Aldrich	Cat#SML2601-5MG
Actinomycin D	Sigma-Aldrich	Cat# A1410-2MG
STM2457	DC Chemicals	Cat#DC53045
FastAP	Thermo Fisher Scientific	Cat#EF0651
Pen-Strep	Biological Industries	Cat#03-031-1B
Geneticin	InvivoGen	Cat#Ant-gn-5
recombinant leukemia inhibiting factor	In house generated	N/A
FastDigest Bcul	Thermo Fisher Scientific	Cat# FD1254
NheI-HF	NEB	Cat# R3131S
FastDigest XmaJ1	Thermo Fisher Scientific	Cat# FD1564
FastDigest Sall	Thermo Scientific	Cat# FD0644
BstBI	NEB	Cat# R0519S
NotI-HF	NEB	Cat# R3189L
HindIII-HF	NEB	Cat# R3104S
Critical commercial assays		
Gateway LR Clonase II	Invitrogen	Cat# 11791-020
PolyJet reagent	SignaGen Laboratories	Cat#SL100688
TransIT-X2 reagent	Mirus	Cat# MIR6003
JET Prime	Polyplus	Cat#101000001
BIO TRI RNA reagent	Bio-lab	Cat# 959758027100
NucleoZOL	Macherey-Nagel	Cat#740404.200
Dynabeads mRNA DIRECT Kit	Life technologies	Cat#61011
Deposited data		
Raw and processed NGS data	This study	GEO: GSE204980
Experimental models: Cell lines		
HEK293T	ATCC	Cat#CRL-3216
MCF7 with genome-integrated Flp-In	kind gift from Reuven Agami (Netherlands Cancer Institute, Amsterdam, The Netherlands)	N/A

(Continued on next page)

Continued

REAGENT or RESOURCE	SOURCE	IDENTIFIER
MCF7	ATCC	Cat#HTB-22
NIH3T3	ATCC	Cat#CRL-1658
V6.5 mESC	From Yonatan Stelzer	Stelzer et al. ⁷¹
mouse embryonic fibroblasts	In house generated	N/A
Oligonucleotides		
Primer and oligo sequences are in Table S1	IDT, Twist Biosciences	Custom
Sequences of the short oligo pool are in Table S2 .	Twist Biosciences	Custom
Sequences of the long, spliced oligo pool are in Table S3 .	Twist Biosciences	Custom
cDNA set (33 samples) are in Table S1 .	90/90 Human ORFeome V1 collection of Gateway Entry Vectors	N/A
Recombinant DNA		
SNRPN-GFP plasmid	In house generated	Uzonyi, Nir, and Schwartz ⁷²
pcDNA5/FRT/TO plasmid	Thermo Fisher Scientific	Cat#V652020
pOG44 recombinase plasmid	Invitrogen	Cat#V600520
pLenti6 V5-DEST gateway vector	Invitrogen	Cat#V49610
Software and algorithms		
STAR/2.7.9a	Dobin et al. ⁷³	https://github.com/alexdobin/STAR
Bedtools multicov	Quinlan and Hall ⁷⁴	https://bedtools.readthedocs.io/en/latest/content/tools/multicov.html
bam2Endreads	Garcia-Campos et al. ²	N/A

RESOURCE AVAILABILITY

Lead contact

Further information and requests for resources and reagents should be directed to and will be fulfilled by the lead contact, Schraga Schwartz (schwartz@weizmann.ac.il).

Materials availability

This study did not generate new unique reagents.

Data and code availability

- NGS data have been deposited at Gene Expression Omnibus (GEO) and is publicly available as of the date of publication with accession number GEO: GSE204980.
- The code for m6Apred-1 and m6Apred-2 is included as supplementary code.
- Any additional information required to reanalyze the data reported in this paper is available from the [lead contact](#) upon request.

EXPERIMENTAL MODEL AND SUBJECT DETAILS

HEK293T (female), MCF7 (female) and NIH3T3 (gender unknown) cells are from ATCC. These cell lines were cultured in DMEM (Gibco) supplemented with 10% FBS and 1% Penicillin and Streptomycin, at 37°C.

For the Y14 dTAG experiments, HEK293T and HEK293T Y14-HA-dTAG cells were maintained in DMEM high glucose (Dutscher) supplemented with 10% of fetal bovine serum (Sigma-Aldrich), and 1% of penicillin and streptomycin (Sigma-Aldrich).

The commonly used V6.5⁷¹ mESC line (male) was kept in DMEM (Gibco) supplemented with 1% Penicillin-Streptomycin, 1 mM L-glutamine, 1% non-essential amino acids, 20% high-grade fetal bovine serum (Biological Industries), beta-mercaptoethanol and 10 µg recombinant leukemia inhibiting factor, at 37°C. Cells were kept on tissue culture plates covered by gelatin (0.2%), in co-culture with in-house generated, radiation-inactivated mouse embryonic fibroblasts.

No cell line authentication was performed.

METHOD DETAILS**Cloning of the short oligo library pool**

The short oligo library pool (related to [Figures 1A–1F](#)) was synthesized by Twist Biosciences and cloned into an SNRPN-GFP plasmid as detailed in.⁷² The full list of sequences in the pool can be found in [Table S2](#).

Design of the short oligo library pool

For the wild type sequences, 200 human and 200 mouse genes were selected based on an annotated methylation site in several miCLIP datasets, aiming to keep a variability of different sequence motifs, as well as different origins of the sites, such as internal exons, end of CDS and 3' UTR. A 50 bp region on both sides of the methylated adenosine was selected based on the hg19 and mm9 genome annotations, leading to a total of 400 sequences with 101 nt length. For the mut-main set, the adenosine at position 51 was mutated to a T. For the mut-secondary set, all As in a DRACH motif, except for position 51 were mutated to a T. For the mut-all set, all As in DRACH motifs were mutated to a T.

The ‘Running mutation’ series is based on 10 human mut-secondary sequences. In this series, 1, 3 or 5 consecutive bases were mutated to their complement, base-by-base, from the first to the last of the 101 nucleotides. The ‘Sequence mutation’ series is based on 4 human mut-secondary sequences. In this set, the extended, 9-mer consensus motif in the middle of the sequence was permuted to all possible combinations of NTNRCNGN, with the methylated A in the middle. The ‘Running methylation’ set is based on ten human mut-secondary sequences. In this set, the extended 9-mer motif was moved from the beginning to the end of the 101 nt sequence, base-by-base. The ‘Motif number’ seq is based on 18 different 9-mer m6A consensus motifs: ATAAACAGT, ATA AACCGT, ATAAACTGT, ATAGACAGT, ATAGACCGT, ATAGACTGT, ATGAACAGT, ATGAACCGT, ATGAACTGT, ATGGACAGT, ATGGACCGT, ATGGACTGT, ATTAACAGT, ATTAACCGT, ATTAACTGT, ATTGACAGT, ATTGACCGT and ATTGACTGT. Each motif was placed in the 101 nt sequence in its wild type form n times (0-8) and in its point mutant (T instead of A in the middle) form 8-n times, at random locations. The remaining bases were filled up with random nucleotides maintaining a 50% GC content.

Each sequence was planned with a unique 10 nt barcode. Barcodes were designed to be devoid of ‘AC’ dinucleotides, to avoid any chance of undergoing methylation, and of purine triplets, as purine rich regions may be promiscuously immunoprecipitated by the anti-m6A antibody.³ Furthermore, barcodes and the planned sequences were designed to be devoid of canonical polyadenylation signals and the restriction sites used in the cloning strategy.

Cloning of the long, splicing oligo library pool

The long oligo pool (related to [Figures 2E–2G](#)) was synthesized by Twist Biosciences. The full list of sequences can be found in [Table S3](#). Each sequence was planned with an 8 nucleotide barcode, with the same considerations as above. Some of the sequences included in the library will be described elsewhere. The single motif set is based on 8 human and 8 mouse sequences. They contain a single 9-mer consensus motif which is moved in steps of four bp from the beginning to the end of the sequence. The double motif set is based on 4 human and 4 mouse sequences. Two consecutive DRACH motifs are moved together through the entire length of the sequence in steps of 8 bp. The length of the variable region of the constructs is 239 bp. With corresponding point mutated zero motif controls, as well as 100 sequences ordered with two different barcodes, the size of the library is 1996 different sequences. With the primers for PCR amplification and restriction sites the entire sequence length is 300 bp. This oligo pool was cloned into the pTwist CMV plasmid, containing the ‘with intron’ version of the *Calm3* gene (ordered from Twist Biosciences), with all DRACH motifs point mutated without disruption of the coding sequence. The majority of the last exon of *Calm3* was replaced with a library placeholder sample sequence for the backbone ordering. The library placeholder was designed to be in between two AvrII restriction sites. We first ensured that the last intron was properly spliced out, following which the placeholder was removed and replaced by the library pool. The library pool was cloned as above, with a traditional restriction-ligation based method. The oligo pool was digested with the restriction enzymes NheI (NEB) and BstBI (NEB), while the plasmid was digested with AvrII (Thermo Fisher XmaJI, complementary to NheI) and BstBI.

Cloning of the *Coa3*, *No12*, and *Calm3* plasmids

DNA sequences encoding the mice *No12*, *Coa3* and *Calm3* genes were ordered from Twist Biosciences. These initial sequences included the full respective ORFs with either 1) the last intron of each gene (three introns for *Calm3*), 2) point mutations of adenosines suspected to be m6A-modified or, 3) no introns. These sequences were PCR-amplified and introduced between HindIII and NotI sites in the pcDNA5/FRT/TO plasmid (Thermo Fisher). For subsequent mutagenesis or modifications, the desired changes were introduced using restriction-free cloning. In brief, the desired changes were introduced using primers with partial complementarity to the original construct being modified. PCRs producing two parts of the new construct with complementary overhangs were conducted. After isolation of the correct products from agarose gels, both PCR products were combined and amplified using terminal primers. The final products were isolated from gels, digested with HindIII and NotI and ligated into a linearized pcDNA5/FRT/TO plasmid (Thermo Fisher). All PCRs were performed using Kapa HiFi DNA polymerase (Roche). Final constructs were partially sequenced using Sanger sequencing. All final sequences are described in [Table S1](#).

Cloning of cDNA constructs

33 cDNA clones encoding full-length ORFs ([Table S1](#)) were selected from the 90/90 Human ORFeome V1 collection of Gateway Entry Vectors. The following criteria were used for selection of the cDNAs: (1) We ensured that the ORF sequence in the clone perfectly matched the ORF sequence as annotated in our assembly, (2) We filtered for genes with >5 exons with ORFs >800 nt, (4) We ensured that the endogenous genes were expressed above the 25% quartile of gene expression in HEK293T cells, to allow comparison of profiles in cDNA to endogenous counterparts, (5) We filtered for genes with experimentally measured m6A gene index (m6A-GIs) >1.8, to ensure that they were endogenously modified somewhere, and (5) We filtered for genes with poor correlations between their predicted m6A profiles on the basis of m6Apred-1 and m6Apred-2 ($r < 0.3$). The cDNAs were cloned into pLenti6 V5-DEST gateway vector (Invitrogen) that was linearized by FastDigest Sall (Thermo Scientific), using Gateway LR Clonase II (Invitrogen), according to the manufacturer's manual. The LR reactions were transformed into chemically competent Stbl3 bacteria (Invitrogen) and grown in 30°.

Cell culture and transfections

For transfection, V6.5 mESCs were seeded on gelatin-covered 6-well plates (without MEF feeder cells) for transfection. *GFP-SLC25A3* plasmid was transfected with the Transit-X2 reagent (Mirus) according to the manufacturer's instructions. Cells were collected 24 h post-transfection.

For the library pool transfection, 0.5 million HEK293T cells were seeded in each well of a 6-well plate. 24 h later cells were transfected with 2 μ g plasmid DNA and 8 μ l home-made PEI reagent. Cells were harvested 24 h post transfection. Each 3 wells of the 6-well plate were merged to form two replicates.

For combined treatment with Actinomycin D and METTL3 inhibitor STM2457 (DC Chemicals, Shanghai, #DC53045), the cells were seeded into 60-mm dishes and grown for one day until 50% confluent. Then, STM2457⁴⁹ compound was added at a final concentration of 5 μ M. After 6 h of incubation, Actinomycin D was added (7.5 μ M) for the indicated time points and the cells were collected after a total treatment of 15 h with STM2457. After lysis, RNA was extracted and RNA sequencing libraries were prepared according to.⁷⁵

Transfections of MCF7 cells were done with JetPrime (Polyplus) reagent, according to the supplier's instructions. Typically, the cells were seeded in 6-cm dishes (Corning) and on the next day transfected with 1-2 μ g of plasmids. The cells were harvested after additional 24 h by scraping and subjected to RNA extraction. For stable expression of reporter genes, MCF7 cells bearing a genome-integrated Flp-In site were transfected with pcDNA5/FRT/TO-encoded genes and pOG44 recombinase in a 1:9 ratio. After 48 h, the medium was supplemented with Hygromycin at 0.1 mg/ml final concentration and grown for three weeks with weekly change of medium.

NIH3T3 cells were seeded on 60 mm plates 24 h prior to transfection. Cells were transfected with pLenti6 cDNA constructs with Lipofectamine 2000 (Thermo Fisher Scientific) reagent according to the manufacturer's protocol. A total of 33 different cDNA plasmids were transfected in pools of 11-12, in duplicates.

Preparation and validation of Y14-HA-dTAG HEK293T cell

The dTAG degron (FKBP12F36V,⁵⁰) was fused in frame into the C-terminus of Y14 in HEK293T using CRISPR-Cas9-mediated knock-in as previously described.⁷⁶ Briefly, 0.6 million of HEK293T cells were co-transfected using JET Prime (Polyplus, 101000001) with 0.25 μ g of each of sgRNAs expressing plasmids and 1.5 μ g of repair plasmid to fuse 3xHA tag and dTAG degron. 24 h post transfection, cells were split in 10 cm dish, and 500 μ g/mL of genetin (G418, InvivoGen) was added after 24 h. CRISPR modification was screened by western blot with Y14 antibody (SantaCruz, 4C4, sc-32312) and HA antibody (Sigma-Aldrich). The selected clones were transfected with Cre expressing plasmid with JET prime to eliminate neomycin resistant gene, and split into a 96 well plate with a single cell per well. Genomic DNA was purified from each clone by SureClean Plus (Bioline, BIO-37047) following manufacturer's instructions. Transgene integration and removal of Neomycin resistant gene were verified by genomic DNA PCR with the primer set F: 5'-TCTGTGTTGCTGGTTGG-3', R: 5'-CCAGGTAACACAGCAAGACC-3'.

dTAG time-course treatment

In a 6 well plate, HEK293T and HEK293T Y14-HA-dTAG cells were cultivated at 70% confluence and treated with DMSO 1:1000 or 50 nM dTAG13 (Sigma-Aldrich) in DMSO, and harvested after 4, 8, 16 and 24 h post-treatment.

For western blot, the following antibodies and dilutions were used: α -GAPDH (Cell Signaling, 14C10, 2118S, rabbit, 1:2000), α -eIF4A3⁷⁰ (Daguenet et al. 2012, 1:1000), α -Y14 (SantaCruz, 4C4, sc-32312, H2416, mouse IgG2b, 1:500), α -MLN51⁷⁰ (Daguenet et al. 2012, 1:1000), α -MAGO (E. Izaurrealde, Max Planck Institute for Developmental Biology, Tuebingen, Germany, affinity purified from rabbit, 1:500).

LC-MS/MS for quantification of m6A/A

The LC-MC/MS sample preparation and analysis was performed as previously described.² In detail, 400 ng of double selected poly-A RNA fractions were digested with 20 units of P1 nuclease (US biological) for 3 h at 50°C in 50 mM ammonium acetate buffer pH 5.3, with 5 mM zinc chloride. Nucleotides were treated with 10 units of CIP (NEB) overnight at 37°C, and then diluted 1:5 in acetonitrile. The samples were dried by acetonitrile evaporation in speedvac. The residue of each sample was re-dissolved in 198 μ L of 0.01%

formic acid. Two μ L of 1 μ g/mL 7-deaza-A were added as internal standard. The mixtures were intensively vortexed (0.5 min), centrifuged (21,000rpm; 5 min), and passed through 0.22- μ m PVDA filters (Millex GV) to 250 μ L inserts of LC-MS vials. The LC-MS/MS instrument consisted of an Acquity I-class UPLC system (Waters) and Xevo TQ-S triple quadrupole mass spectrometer (Waters) equipped with an electrospray ion source and operated in positive ion mode was used for analysis of nucleosides. MassLynx and TargetLynx software (version 4.1, Waters) were applied for the acquisition and analysis of data. Chromatographic separation was done on a 100 mm \times 2.1 mm internal diameter, 1.8- μ m UPLC HSS T3 column equipped with 50 mm \times 2.1 mm internal diameter, 1.8- μ m UPLC HSS T3 pre-column (both Waters Acquity) with mobile phases A (0.01% formic acid) and B (50% aqueous acetonitrile with 0.01% formic acid) at a flow rate of 0.2 mL/min and column temperature 25°C. A gradient was used as follows: the column was held at 0% B for 1 min, then a non-linear increase (curve 8) to 35% B from 1 to 18 min, then a non-linear increase (curve 8) to 100% B 18–18.2 min, held at 100% B 18.2–19 min, back to 0% B 19–20 min and equilibration at 0% B for additional 5 min. Samples kept at 7°C were automatically injected in a volume of 1 or 3 μ L, to get non-saturated A and m6A signals, respectively. Retention times were 9.7, 11.4, 11.8, and 13.8 min for 7-deaza-A, G, A, and N6-Me-A respectively. For mass spectrometry, argon was used as the collision gas with a flow of 0.10 mL/min. The capillary voltage was set to 2.67kV, source temperature 150°C, desolvation temperature 400°C, cone gas flow 150L/h, desolvation gas flow 800L/h.

Nucleoside concentration was calculated using a standard curve of the relevant nucleotide concentration in each sample. Standard curves included increasing concentration of all measured nucleosides ranging from 0–1000 ng/mL that were positioned at the beginning and at the end of each run. All the calculated values for the different nucleosides in each sample fell within the standard curve range. The compounds were detected in positive mode as multiple-reaction monitoring, with the following parameters: 267.1 > 118.1 and 267.1 > 135.0 m/z (collision energy CE 57 and 16 eV respectively) for 7-deaza-A, 284.2 > 152.1 m/z (CE 14eV) for G, 268.1 > 136.1 m/z (CE 15 eV) for A, and 282.1 > 123.1 and 282.1 > 150.1 m/z (CE 40 and 25 eV respectively) for N6-Me-A.

SCARLET analyses for quantification of m6A/A

SCARLET analyses of mRNA samples (1 μ g each) were performed as previously described,² except that two-dimensional thin-layer chromatography (TLC) was used to finally resolve the 5'-monophosphate nucleosides (first dimension solvent: 66% isobutyric acid, 0.25% ammonia; second dimension solvent: 68% 2-propanol, 6.4% hydrochloric acid).⁷⁷ The use of two-dimensional TLC resulted in superior separation of A and m6A from the “background” of other nucleosides.

RNA extraction, m6A IP, and library preparation

RNA from mESC, NIH/3T3 and HEK293T cells was extracted with NucleoZOL (Macherey-Nagel); from MCF7 cells BIO TRI RNA reagent (Bio-lab) was used. RNA was poly-A selected with oligo dT-beads (Dynabeads mRNA DIRECT Kit, life tech). For all single-plasmid transfections, sample pooling, m6A immunoprecipitation and NGS library preparation was prepared according to the step-by-step m6A-seq2 protocol described in.¹⁵ m6A IP and amplicon library preparation of the oligo library pool was performed on the basis of the same protocol with the following modifications: the 3' adapter ligation and pooling steps were omitted, the 5' adapter ligation step was omitted, reverse transcription was performed with a sequence specific RT primer (Table S1), library amplification was performed with sequence specific PCR primers containing Illumina sequencing adapters (Table S1). All NGS libraries were sequenced on the Illumina NovaSeq 6000 platform.

Datasets analyzed in this study

Measurements of m6A in WT A549 and in counterparts depleted of WTAP, METTL3, METTL14, and KIAA1429, as well as from mouse dendritic cells and embryonic fibroblasts, were obtained from³⁴ (GSE54365). Measurements of m6A in WT and METTL3 KO mESCs were obtained from,² (GSE122961, replicate 1). mRNA stability in WT human MCF7 cells were obtained from⁴⁸ (GSE49831). mRNA stability in WT and METTL3 KO mESC cells were obtained from.¹⁴ Deadenylation rates were obtained from.⁴⁶

Compilation of m6A catalogs at single nucleotide resolution

For the assembly of a high-confidence catalog of m6A sites in human cells employed in Figure 3D, we collected m6A catalogs from the following sources: (1) A catalog of 81,519 sites identified across at least one of six miCLIP sites, assembled in,³⁵ (2) A set of 12,672 m6A sites identified via DART-seq,³⁷ (3) A set of 45,616 sites identified via SAC-seq, pooled from measurements conducted in HepG2, HEK293 and HeLa cells, which were downloaded from GSE162356, (4) A set of 36,552 sites identified in HEK293 cells using miCLIP2,⁴⁰ (5) A set of 170,240 sites identified in HEK293 cells via GLORI.⁴¹ The UCSC ‘LiftOver’ tool was used to convert hg38 coordinates to hg19, when needed. We then generated a dataset of all eligible DRACH motifs within 7,300 gene-bodies (filtered based on expression level). Each motif was annotated with its predicted methylation status on the basis of m6Apred-2, following which it was merged with the assembly of m6A sites to allow assessment of experimentally-defined m6A status.

Alignment and calculation of IP/input enrichment scores

Oligo pools

Oligo pool data was analyzed with a custom R script. Enrichment scores were calculated as the ratio between the number of reads originating from a single sequence upon m6A-IP in comparison to the input and normalized to the median score of all human, mouse and synthetic constructs with no m6A consensus motif in the corresponding library.

To calculate the delta enrichment scores at each position for **Figure 1D**, from the mean enrichment score of a given nucleotide we subtracted the mean enrichment score of any other nucleotide. These scores were averaged for all the different motif permutations for each position.

Constructs

Transcriptome wide m6A-seq2 datasets were mapped to mm9 or hg19 genome assembly and the transfected plasmid using STAR/2.7.9a.⁷³ Per-base read coverages were obtained with txtools (<https://github.com/AngelCampos/txtools>), and normalized to the total number of reads in the pool. Raw input and IP read counts were first normalized by the sum of reads across the entire corresponding pool of samples subjected to m6A-seq simultaneously (i.e. across all input samples or all IP samples, respectively). m6A enrichment levels were calculated as the fold-change in normalized coverage at the modified position between IP and input. For constructs with large insertions and deletions (in **Figures 2H** and **2I**), we sought to avoid contribution of signal originating from the insert (or from upstream intronic regions). In these analyses we therefore constrained the analysis of input and IP reads only to ones overlapping the sites and beginning at most n bases upstream of the methylated position. In the case of **Figure 2H**, n = 10 was employed, given the presence of a DRACH motif 10 nt upstream of the shortest construct (in which the targeted m6A site was 29 nt away from the splice junction). To quantify the constructs with intron retention (**Figure 2I**), n = 40 was employed; In this case a longer distance could be used, allowing integration of more signal, without reaching the DRACH site.

Transcriptome-wide

m6A-seq measurements (IP and input) were aligned against the hg19 and mm9 genomes for human and mouse, respectively, using STAR/2.7.9a.⁷³ An in-house script was employed to map the genomic coordinates to transcriptomic annotations. For these annotations, we used canonical ‘UCSC Known Genes’ for human and mouse. Only reads fully matching a transcript structure were retained. Paired end reads were computationally extended in transcriptome space from the beginning of the first read to the end of its mate, and coverage in transcriptome-space was calculated for each nucleotide across all transcripts. For each base along each transcript, an IP/input enrichment score was calculated.

Implementation of m6Apred-1 and m6Apred-2 models

Gene models for roughly 20,000 ‘canonical’ human and mouse genes were downloaded from the ‘UCSC Known Genes’ annotation table in the UCSC genome browser. For each gene we identified all ‘eligible’ DRACH motifs, and furthermore recorded their distance from the nearest exon-intron junction. In m6Apred-1, each of the motifs was considered methylated. In m6Apred-2, an eligible DRACH motif was only considered methylated if its distance to the nearest splice junction exceeded 100 nt. With the exception of analyses in **Figure S5C**, also motifs within 100 nt from the transcript start or end site were considered non-eligible by m6Apred-2, based on the finding that m6A is also depleted in the vicinity of polyadenylation sites. To mimic the regional enrichment in m6A-seq, every site predicted to undergo methylation was modeled as a Gaussian over a 200 bp region centered at the methylated site. The values along this Gaussian were derived using the density function of a Gaussian distribution (mean = 0, SD = 4), which were calculated for 100 values distributed at fixed intervals between 0 and 9 using the dnorm() function in R, and min-max normalized, to distribute between 0 and 1. The final predicted enrichment value at each position along the gene was defined as the sum of all signals (stemming from zero, one or potentially multiple gaussians) overlapping this position (see Supplementary code).

For the analyses summarizing gene-level predicted or measured methylation levels, we calculated the mean signal over gene bodies. Gene bodies were defined as the entirety of the gene excluding TSS-proximal regions (first 200 bp of the gene) and distal 3' UTR regions (greater than 400 bp from the stop codon). These regions were excluded to avoid contribution from signal originating from m6Am at the beginning of genes^{34,42–44} and overcome limitation in available annotations of 3' UTRs (see **results**). The gene-level quantification of experimentally-measured m6A levels was calculated as the overall number of reads per gene-body in the IP experiment divided by the corresponding number in the input experiment. This metric draws on our previously developed m6A-gene index (GI).¹⁵

For assessing agreement between predicted and experimentally measured profiles, we only included protein-coding genes with an average coverage per base exceeding 5 reads in the Input sample, to ensure adequate expression for estimating enrichment levels. These filters typically allowed quantifications of ~5000–~10000 genes.

For a rough approximation of 3' termini on the basis of ‘input’ RNA-seq data, we used a strategy similar to the one employed in.³ We scanned the 3' UTRs from 5' to 3', and defined the 3' UTR as the first point at which coverage dropped >3-fold with respect to median coverage within the open reading frame of the gene.

Analysis of METTL3 inhibitor RNA degradation timepoints

METTL3 inhibitor and actinomycin D treated samples were mapped to hg19 genome annotation using STAR/2.7.9a.⁷³ Total read count per gene was computed with bedtools multicov,⁷⁴ with the samples ordered as non-treated 0 h replicates, 3 h replicates, 6 h replicates, 9 h replicates, followed by the treated samples ordered similarly. Genes with less than a sum of 100 reads for all inhibitor treated and control timepoints were filtered out. Read counts were normalized to library size. Read counts were log transformed and the decay rate was calculated as a linear model fit on all time point duplicate measurements for treatment and control. Genes that had an r^2 value of the fit below 0.5 were filtered out. Remaining decay rates were correlated with measured and predicted m6A levels, as well as exon density.

Analysis of Y14 degron timepoints m6A IP data

The reads were aligned with STAR/2.7.9a to the hg19 genome. For further analysis, the BAM files were filtered for uniquely aligned reads and processed by the bam2Endreads Rscript² for RNA fragment coverage in transcript space, based on the UCSC hg19 canonical gene annotation. M6a-GI and m6A-site score1 calculation were performed according to Dierks et al. (2021).¹⁵ High confidence m6A-sites were defined as *de-novo* detected m6A-peaks in which the summit has an absolute distance to the nearest DRACH motif with less than five bases (see below, *De-novo* m6A peak calling).

***De novo* m6A peak calling**

m6A peak calling was performed as in,³ with minor adaptations. Genes were filtered for sufficient coverage for m6A peak detection with a threshold of at least five reads median coverage in the input sample. For a 51 bases rolling window centered around each base of an annotated transcript, the m6A site-score 2 was determined, defined as the ratio of the mean m6A-IP coverage of the window against the median IP. An Enrichment-Window was defined when m6A-site score 2 exceeded four for 15 consecutive bases. For each detected Enrichment-Windows, the Winscore was calculated by dividing the IP-derived m6A site score 2 by the same metric based on the Input coverage. Enrichment-Windows with a Winscore >2 were isolated and consecutive windows merged. The final m6A-peak criteria was an IP to Input coverage fold-change of >3. High-confidence single-nucleotide m6A-sites were defined by the summit of an m6A-peak with a maximum absolute distance of five bases to the closest adenosine of a DRACH motif.

QUANTIFICATION AND STATISTICAL ANALYSIS

All statistical analysis was done in R. Analysis details can be found in figure legends and the result sections. Figures were prepared with basic R package and ggplot2.